Cryptic arsenic cycling controls oxygenic photosynthesis in Precambrian-analog microbial mats

Andrea Castillejos Sepúlveda[1,*], Daan R. Speth[2,3], Carolin Kerl[4], Daniel Doherty-Weason[5,6,7], Federico A. Vignale[8], Kinga Santha[1], Wiebke Mohr[2], Arjun Chennu[1,9], Elisa Merz[1,10], Dirk de Beer[1], Maria E. Farias[11], Judith M. Klatt[1,5,6,7*].

[1] Microsensor Group, Max Planck Institute for Marine Microbiology, Bremen, Germany.

[2] Biogeochemistry Group, Max Planck Institute for Marine Microbiology, Bremen, Germany.

[3] Division of Microbial Ecology, Centre for Microbiology and Environmental Systems Science, University of Vienna, Vienna, Austria.

[4] Environmental Geochemistry, Bayreuth Center for Ecology and Environmental Research (BayCEER), University of Bayreuth, 95440 Bayreuth, Germany

[5] Microcosm Earth Center, University of Marburg & Max Planck Institute for Terrestrial Microbiology, 35032 Marburg, Germany

[6] Center for Synthetic Microbiology (SYNMIKRO), 35032 Marburg, Germany

[7] Biogeochemistry Group, Department of Chemistry, University of Marburg, 35032 Marburg, Germany

[8] European Molecular Biology Laboratory - Hamburg Unit, Hamburg 22607, Germany

[9] Australian Institute of Marine Science, Townsville, Australia

[10] University of Konstanz, Plant Ecophysiology, University of Konstanz, Germany

[11] PUNABIO S.A. Campus USP-T Av. Solano Vera y Camino a Villa Nougués, San Pablo, Tucumán, Argentina

*Correspondence: andreacas@web.de, Judith.Klatt@mpg.mpi-marburg.de

Abstract

The delayed rise of atmospheric oxygen, despite the early evolution of oxygenic photosynthesis (OP), remains a central puzzle in Earth history. Numerous ecological and geochemical constraints on OP have been proposed, but the role of environmental stressors at the physiological and ecosystem level is poorly understood. Here we show that Chl-*f*-harboring cyanobacteria in a high-altitude Andean microbial mat – an analog for Precambrian ecosystems – switch from OP to arsenite-driven anoxygenic photosynthesis (AP) under high light. Using microsensor profiling, mat incubations, and metatranscriptomics, we show that this shift is triggered by the accumulation of reactive oxygen species (ROS), especially hydrogen peroxide, which suppresses OP. Instead of ceasing activity, cyanobacteria reroute electron flow, using arsenite as the electron donor to sustain photosynthesis while avoiding both intracellular ROS from OP and extracellular ROS from aerobic arsenite oxidation. This switch is reversible and coordinated with diel cycles of light and arsenic speciation, sustained by a cryptic arsenic redox cycle, continuously regenerating arsenite for AP. Although the enzymatic basis remains unresolved, these findings reveal a hidden layer of metabolic plasticity in cyanobacteria and suggest that oxidative stress-responsive metabolic shifts may have supported early phototroph survival while limiting oxygen release – potentially contributing to Earth's protracted oxygenation.

Main

The evolution of oxygenic photosynthesis (OP) in cyanobacteria was a transformative event in Earth's history, fundamentally reshaping our planet. OP likely emerged during the Archean eon (3.7–2.5 billion years ago), within microbial mats – layered microbial communities that dominated shallow waters[1-3]. Before the rise of OP, light-driven microbial primary production relied on anoxygenic photosynthesis (AP), which uses reduced substances such as ferrous iron or sulfide as electron donors for carbon fixation[4,5]. These metabolisms shaped early biogeochemical cycles and may have delayed the proliferation of OP across Earth's surface[6-8].

Intriguingly, some modern cyanobacteria are capable of both OP and AP, using sulfide as preferred electron donor when available[9-14]. Thus, it has been proposed that even early cyanobacteria may have

already transitioned between modes of photosynthesis in response to environmental cues. However, the evolutionary timeline of photosynthetic versatility and the extent to which such flexibility influenced the evolutionary trajectory of OP remains unclear[15,16].

Arsenite (AsO_3^{3-}, As(III)), a reduced and bioavailable form of arsenic, was abundant in Archean and Proterozoic environments due to intense volcanic activity[17,18]. Like sulfide, As(III) can serve as an electron donor for AP in obligate anoxygenic phototrophs and can fuel a complete microbial arsenic redox cycle[19,20]. In cyanobacteria, arsenic and sulfur metabolism are co-regulated, suggesting an evolutionary connection[21]. Despite this link and arsenic's environmental relevance, the role of arsenic in modulating early photosynthesis remains poorly understood.

One likely setting for the emergence of cyanobacteria is microbial mats, where they would have navigated steep chemical gradients, intense ultraviolet (UV) radiation, and reduced, often toxic, compounds like As(III). We hypothesize that As(III) availability may have influenced the balance between AP and OP – either by providing an alternative electron donor or by chemically interfering with the efficiency and evolution of OP. Arsenic could have thereby acted as both a metabolic substrate and a physiological stressor, shaping the evolutionary trajectory of early phototrophs.

To address this, we studied microbial mats from Laguna Pozo Bravo, a high-altitude hypersaline lake in the Central Andes that serves as a modern analogue to Precambrian mat ecosystems. Combining high-resolution microsensor profiling with incubation experiments and multi-omics approaches, we investigated how local arsenic speciation affects photosynthesis within these layered communities. Our findings provide new insights into the metabolic plasticity of cyanobacteria under extreme environmental stress and reveal previously unrecognized mechanisms by which arsenic may have constrained the early expansion of OP.

A Precambrian-analog microbial ecosystem in the high Andes

Microbial mats are among the oldest known ecosystems on Earth, and modern analogs found in extreme environments offer valuable windows into early microbial life Earth[3,22-26]. Laguna Pozo Bravo,

a hypersaline lake in the Central Andes (~3300 m elevation), is one such system[27-29]. Its high UV radiation, extreme temperature fluctuations, and elevated arsenic levels – due to the volcanic origin of the surrounding geology – recreate conditions believed to be common in shallow aquatic environments of the Precambrian eon[27,29,30].

In February 2019 and January 2023 the lagoon floor was extensively covered by cohesive, light pink microbial mats, thriving underneath a hypersaline (137.25 g L^{-1}) water column with a stable temperature around 20°C. The mats formed stable sheets atop coarse sediment and displayed clear vertical stratification into four visible layers: a light pink upper crust rich in calcium carbonate, a green layer, a red layer, and a brown layer (Fig. 1a, inset).

To identify the key phototrophic groups across these layers, we combined hyperspectral imaging with metagenomic analysis. Despite recovering only three cyanobacterial bins – *Halothece* sp., ESFC-1 (*Spirulinaceae*) and RECH01 (*Elainellaceae*) – from the metagenomes (Extended Data Fig. 1, Suppl. Results 1), hyperspectral data confirmed that cyanobacteria were the dominant phototrophs in the mat. The green layer was dominated by Chl *a* (absorption maximum λmax≈690 nm) and phycocyanin (λmax≈625 nm) indicative of cyanobacteria[31-33]. This layer also included a zone dominated by BChl *a* (λmax≈810 nm), indicative of purple anoxygenic phototrophs[34] (Fig. 1c). The red layer showed a clear absorption maximum at 715 nm, characteristic of BChl *e* in green anoxygenic bacteria like Chloroflexi[35] or Chl *f* in cyanobacteria[36].

Metagenome screening revealed a great variety of arsenic-related genes at levels comparable to housekeeping genes (Fig. 1c&d, Suppl. Results 2), suggesting arsenic metabolism is a core function of the mat community. Indeed, the total dissolved inorganic arsenic concentration in the water column was 6.9+/-0.4 µM, toxic to most life but substantially below levels in well-studied arsenic-rich ecosystems, such as Mono Lake[19,37].

Far-red light and dual-layer oxygenic photosynthesis

In-situ microsensor depth profiling revealed that OP occurred in two distinct mat layers. An upper oxygen concentration peak was observed at ~1 mm depth (Fig. 2a&d, Extended data Fig. 2) in the green Chl *a*-dominated layer (Fig. 1b). An additional net OP maximum was observed at approximately 2-3 mm depth (Fig. 2a&d, Extended data Figs. 2, 3), coinciding with the red layer that exhibited an absorption peak characteristic of far-red pigments, consistent with either BChl *e* or Chl *f*. The detection of net oxygen production indicates a cyanobacterial origin, strongly suggesting Chl *f*, since anoxygenic phototrophs do not evolve oxygen. This spectral adaptation aligns with previously described strategies in cyanobacteria that extend photosynthesis into low-energy light environments[38-41]. These traits are believed to have evolved to support photosynthesis in shaded, low-energy environments – such as those within microbial mats – possibly already in the Precambrian[42].

Diel arsenic cycling aligns with photosynthetic shutdown in deep mat layers

Microbial mats typically sustain continuous OP throughout daylight hours. However, in Pozo Bravo we observed an unusual diel pattern: OP declined in both phototrophic layers, and was even completely interrupted around midday in the deeper Chl *f*-dominated zone, despite ongoing light availability (Fig. 2a&d, Extended data Figs. 2, 3). This abrupt shutdown suggested that environmental stressors and/or metabolic transitions may regulate photosynthetic activity.

To investigate this, we monitored diel changes in key redox-sensitive compounds – arsenic, hydrogen sulfide, and iron – within the mat's photic zone. Neither H_2S nor Fe(II) exhibited depth profiles or temporal dynamics consistent with phototrophic utilization (Supplementary Results 3). In contrast, arsenic speciation displayed pronounced, light-correlated shifts: As(III) dominated under dark conditions, while up to 98% of the dissolved arsenic pool was oxidized to arsenate (AsO_4^{3-}, As(V)) during the day (Fig. 2b,c). These dynamics were strongest within the top centimeter, where both cyanobacterial layers reside.

121 Strikingly, the peak in As(V) concentration coincided with the timing and depth of maximal OP
122 inhibition in the deeper layer. This alignment suggests a potential causal link between arsenic redox
123 transitions and photosynthetic regulation – specifically, that either arsenic itself or its light-driven
124 oxidation may contribute to stress or otherwise disrupt OP, particularly in far-red light-adapted
125 cyanobacteria.

126 **Reactive oxygen species link arsenic and light to photosynthetic inhibition**

127 To study the effect of arsenic on OP, we performed ex-situ incubations of intact mat sections under
128 varying light intensities, with and without added As(V). In arsenic-free conditions, oxygen production
129 increased and stabilized under both low and high light, as expected for typical cyanobacterial mats
130 (Extended Data Fig. 4). However, when 10 µM As(V) was added, oxygen production initially rose but
131 then abruptly ceased after ~30 minutes of high-light exposure (~1000 µmol photons m^{-2} s^{-2}). Oxygen
132 production resumed when light intensity was reduced.

133 This response occurred independently of the time of day or duration of light exposure, indicating that
134 OP suppression was not due to cumulative photoinhibition or diel rhythm, but instead resulted from a
135 combined effect of high light and arsenic. Although most mat pieces did not exhibit the distinct double
136 peaks observed in-situ, occasionally two net productivity maxima were observed. Notably, the
137 response was most pronounced in deeper mat layers, mirroring in-situ patterns and suggesting that
138 the Chl *f*-dominated community is particularly sensitive to this stressor combination.

139 To elucidate the mechanism behind OP inhibition, we simultaneously measured depth profiles of H_2O_2,
140 a key ROS, under varying light and arsenic conditions (Fig. 3). Without arsenic, no net production of
141 H_2O_2 was observed across light intensities. In As(V)-treated mats, H_2O_2 concentration within the
142 photosynthetically active zone dramatically increased at 1000 µmol photons m^{-2} s^{-1}. Upon the cessation
143 of OP, H_2O_2 concentration dropped back to baseline levels. These dynamics suggest that ROS
144 accumulation acts as a physiological signal or threshold, triggering the shutdown of OP in
145 cyanobacteria to avoid further oxidative damage.

146 Transcriptomic data from mats sampled in-situ across the diel cycle supported this interpretation (Fig.
147 5, Suppl. Results 4). Genes associated with oxidative stress and ROS defense – such as catalases,
148 thioredoxins, and the phage shock protein *pspA* – were upregulated during mid-morning and around
149 noon, coinciding with peak light and As(V) levels (Fig. 5b, Extended Data Fig. 7). Expression of key stress
150 response genes like *pspA* and *hsp70* was detectable in the bin RECH01, consistent with membrane
151 disturbance and ROS-mediated stress[43,44].

152 While Pozo Bravo mats likely experience continuous oxidative pressure due to high irradiance and OP
153 itself, the shift to net H_2O_2 accumulation suggests that sink capacity is overwhelmed under combined
154 arsenic and light stress. Experimental addition of H_2O_2 confirmed that the mats can normally buffer
155 external ROS: even at 200 µM H_2O_2, oxygen production remained unaffected and the compound was
156 rapidly consumed in the upper layers (Extended Data Fig. 5), as also observed in other mat systems[14].
157 Thus, the observed H_2O_2 spike likely represents a breakdown of ROS homeostasis.

158 To identify possible sources of this ROS burst, we treated mats with both As(V) and DCMU, a PSII
159 inhibitor that blocks OP. Even under these conditions, transient H_2O_2 production occurred at the oxic
160 interface (Fig. 3f), indicating that OP is not the sole ROS source. Likely contributors include abiotic
161 As(III) oxidation, light-driven ROS formation via iron photochemistry[45], and singlet oxygen production
162 during photosystem repair[46]. The reaction of As(III) with oxygen to form As(V) and H_2O_2 according to

163 $$H_3AsO_3 + 2H_2O + O_2 \rightarrow H_3AsO_4 + H_2O_2 \qquad (\Delta G° = -40.82 \text{ kcal mol}^{-1}) \qquad (1)$$

164 is thermodynamically favorable and may proceed both enzymatically and abiotically[47].

165 Thus the combination of high light and dissolved arsenic induces local H_2O_2 accumulation that
166 overwhelms the mat's ROS-scavenging capacity, triggering a shutdown of OP – particularly in the
167 deeper, far-red light-adapted cyanobacterial layer. This photophysiological response suggests a tightly
168 regulated transition to an alternative metabolic mode under oxidative stress. Given the synchronous
169 depletion of oxygen and accumulation of As(V), we hypothesized that the cyanobacteria switch to AP
170 using As(III) as an alternative electron donor.

171 **Cyanobacteria perform arsenite-driven anoxygenic photosynthesis**

172 To test whether cyanobacteria in Pozo Bravo mats can use As(III) for AP, we incubated mat pieces
173 under various light wavelengths and inhibitor conditions over a diel cycle. The photosynthetic inhibitor
174 DCMU was used to block PSII and thereby oxygenic activity, allowing us to detect only AP driven
175 processes (Fig. 4, Extended data Fig. 6).

176 In these incubations, we consistently observed net reduction of As(V) in the dark, likely by microbial
177 respiration using As(V) as a terminal electron acceptor. Upon illumination, net reduction rates
178 decreased, but in most cases, we did not observe net oxidation of As(III) – showing co-occurrence of
179 light-driven As(III) oxidation and continued As(V) reduction. We thus estimated photosynthetic As(III)
180 oxidation rates by correcting the net conversion for background As(V) respiration (Fig. 4a,d, See
181 Methods).

182 These gross rate calculations revealed that light-driven As(III) oxidation occurred under all tested light
183 conditions (Fig. 4). The highest rates were observed in white light without DCMU, consistent with
184 aerobic oxidation using photosynthetically produced oxygen. However, gross oxidation persisted even
185 in DCMU-treated samples – where OP was blocked – demonstrating true AP (Fig. 4b, Extended Data
186 Fig. 6).

187 Light-quality experiments helped identify the phototrophs involved. At 810 nm, AP could be attributed
188 to purple sulfur bacteria, as previously observed in cultures[19,37] and in mats[22]. As(III) oxidation also
189 occurred at 690 nm and 715 nm – wavelengths specific to cyanobacterial Chl *a* and Chl *f*, respectively.
190 Crucially, gross oxidation was observed at these wavelengths in the presence of DCMU, strongly
191 implicating cyanobacteria in As(III)-driven AP.

192 The transition dynamics between AP and OP differed markedly between exposures to 690 nm and
193 715 nm, suggesting that distinct cyanobacterial groups with different adaptations to As(III) were
194 involved. The response at 690 nm followed a classic transition pattern, previously observed in
195 cyanobacteria capable of sulfide-driven AP[10]: OP resumed only after As(III) was depleted. Thus Chl *a*-

196 cyanobacteria initially performed AP and later switched to OP once the electron donor As(III) was
197 exhausted (Extended Data Fig. 6d–i).

198 At 715 nm, a distinct biphasic pattern emerged, mirroring in-situ diel dynamics (Fig. 4a,c,e, Extended
199 data Fig. 6l-q). During the first hours of illumination (phase 1), OP dominated and As(III) oxidation was
200 low - an unexpected outcome given the high availability of electron donor for AP. Later (phase 2), OP
201 ceased and As(V) production sharply increased, both in DCMU-treated and untreated samples (Fig. 4e).
202 These patterns strongly support a delayed functional switch from OP to As(III)-driven AP by Chl *f*-
203 containing cyanobacteria. This transition appears to require the combined presence of As(III), light,
204 and oxygen, the latter accumulating only after prolonged illumination of the incubation vials.

205 Mechanistic insights into As(III)-driven AP was hindered by the low metatranscriptomic coverage of
206 cyanobacterial bins. Although several arsenic-related stress and efflux genes (*arsA*, *arsB*, *acr3*[48]) were
207 expressed (Extended Data Fig. 7), canonical As(III) oxidation genes (*aioAB*[49]) were not detected. This
208 suggests that As(III) oxidation may involve divergent enzymes, or a fundamentally different
209 biochemical pathway. Repeated attempts to isolate cyanobacterial strains capable of As(III)-driven
210 photosynthesis were also unsuccessful, ultimately preventing mechanistic characterization of this
211 process.

212 However, diel transcription of photosystem genes revealed dynamic regulation: PSI genes peaked in
213 the morning, while PSII expression increased later in the day. The PSII core gene *psbA*, encoding D1,
214 peaked shortly before OP resumed in the afternoon (Extended data Fig. 7b). Given that Chl *f* synthesis
215 requires the replacement of D1 with a Chl *f*-specific isoform that inhibits PSII[50,51], this expression
216 pattern may suggest a regulatory mechanism by which cyanobacteria suppress OP and favor PSI-based
217 AP under stress, then reassemble PSII to restore OP as conditions improve.

218 Together, these results provide strong indirect evidence that cyanobacteria in Pozo Bravo mats can
219 perform As(III)-driven AP, particularly under far-red light and when OP is suppressed. This metabolic

220 flexibility likely helps mitigate intracellular oxidative stress during periods of high light and arsenic
221 exposure.

222 **A cryptic microbial arsenic cycle sustains phototrophic activity**

223 The presence of As(III)-driven AP in the cyanobacteria-dominated mats of Laguna Pozo Bravo raises a
224 key question: how is As(III) supplied during daylight hours, when in-situ measurements show that
225 nearly all dissolved arsenic is present as As(V)? In this scenario, AP must rely on a continuous local
226 supply of As(III). We therefore investigated how the broader microbial community sustains this
227 process.

228 First, we examined metatranscriptomic profiles of arsenic redox cycling genes across the diel cycle.
229 Focusing first on the oxidative side, transcripts of the canonical arsenite oxidase genes *aioA* and *aioB*
230 were detected in several non-cyanobacterial taxa, including members of the Rhodobacterales
231 (Alphaproteobacteria) and Chromatiales (Gammaproteobacteria), both including purple anoxygenic
232 phototrophs and chemolithotrophs (Fig. 5b). These groups showed peak *aioAB* expression during
233 daytime, coinciding with periods of active AP and elevated As(V) levels. This supports the notion that
234 As(III) oxidation is a widespread phototrophic function within the mat.

235 To explore how As(III) remains available for As(III)-driven AP despite its low measured concentration,
236 we examined the expression of genes involved in As(V) reduction, including *arsC*, *gapdh*, and *arsD*,
237 which support both detoxification and respiratory pathways[52-54] (Fig. 1). These genes, along with *arsA*,
238 *arsB*, *acr3*, and *arsJ* (involved in As(III) efflux[48,52]), were transcribed throughout the diel cycle, with *arsC*
239 expression peaking during the day (Fig. 5a). This suggests that As(III) is regenerated within the photic
240 zone via continuous microbial As(V) reduction, effectively sustaining As(III)-dependent phototrophy
241 even when As(V) dominates the bulk porewater.

242 Measured rates of As(V) reduction in incubation experiments supported this interpretation. Reduction
243 rates scaled linearly with As(V) concentration up to ~19 µM, showing no signs of saturation (Fig. 4d).
244 These first-order kinetics are consistent with low-affinity reduction systems operating efficiently at

245 ambient concentrations and suggest that As(III) production is dynamically coupled to its phototrophic
246 oxidation. As a result, arsenic cycling within the mat is a cryptic redox loop, where As(V) is continually
247 reduced and re-oxidized, enabling AP even under oxidizing conditions (Suppl. Results 5).

248 **A daily cycle of arsenic-driven photosynthesis and stress regulation**

249 The microbial mats of Laguna Pozo Bravo operate as tightly regulated ecosystems in which
250 phototrophic activity, arsenic redox cycling, and environmental stress responses are intricately linked.
251 Over the course of a diel cycle, different microbial groups contribute to and are shaped by the dynamic
252 chemistry of arsenic and light (Fig. 6).

253 In the early morning, both cyanobacterial layers – those dominated by Chl *a* and Chl *f* – perform OP,
254 producing oxygen and initiating the oxidation of As(III) to As(V). Anoxygenic phototrophs, including
255 purple bacteria and possibly some Chl *a* cyanobacteria, also become active, performing AP using
256 residual As(III) as an electron donor. In parallel, heterotrophic respiration with As(V) maintains a cryptic
257 redox loop, releasing As(III) back into the mat and sustaining phototrophic arsenic cycling.

258 By midday, environmental stress peaks. High irradiance, and increasing aerobic As(III) oxidation to
259 As(V) coincide with a measurable rise in H_2O_2. This oxidative stress triggers a shutdown of OP in the
260 deeper, Chl *f*-dominated cyanobacteria, while surface-layer Chl *a* cyanobacteria maintain reduced OP
261 rates, and possibly As(III)-driven AP sustained by the rising As(V) reduction rates. The deeper
262 phototrophs transition completely to As(III)-driven AP.

263 In the late afternoon, light levels decrease and Chl *f* cyanobacteria gradually resume OP, completing
264 the cycle. This synchronized sequence of OP, AP, and arsenic redox cycling supports a metabolically
265 flexible community that responds dynamically to fluctuating light and chemical conditions. It highlights
266 the ecological importance of arsenic – not just as a toxin or redox substrate, but as a regulating force
267 in the coordination of microbial energy metabolism.

268 **Arsenic-mediated suppression of photosynthesis may have delayed planetary oxygenation**

269 Although OP by cyanobacteria likely evolved during the Archean, it took hundreds of millions of years
270 for atmospheric oxygen to accumulate substantially, culminating in the Great Oxidation Event (GOE)
271 ~2.5–2.3 billion years ago[55]. The reasons behind this lag remain debated, often in terms of ecological
272 or geochemical limitations – such as nutrient scarcity, Fe(II)-driven AP competition, or inefficient
273 organic carbon burial[7,8,56]. Our findings suggest an additional, previously unrecognized factor: arsenic
274 could have directly suppressed OP in early microbial ecosystems.

275 In modern Precambrian analogs at Pozo Bravo, we observed that cyanobacteria dynamically
276 transitioned from OP to As(III)-driven AP. This shift was not driven by substrate depletion or light
277 limitation, and appears to reflect a physiological response to oxidative stress rather than a passive
278 metabolic fallback. When ROS levels rise cyanobacteria suppress OP – but instead of halting
279 phototrophy, they re-route electron flow to perform AP with As(III) as the electron donor. This
280 strikingly adaptive strategy avoids intracellular ROS from PSII activity and extracellular ROS generated
281 by As(III) oxidation in the presence of oxygen (Eq. 1), while maintaining energy conservation. Such
282 plasticity likely conferred a major advantage in early Earth environments, where UV stress, metal
283 toxicity, and redox fluctuations were pervasive, positioning As(III)-driven AP as a purposeful stress-
284 avoidance strategy rather than an evolutionary relic.

285 This strategy comes at a cost for the ecosystem's net oxygen budget – as AP does not release oxygen.
286 Notably, the mitigation of OP does not require high arsenic levels, because tight redox recycling
287 maintains As(III) availability. Such cryptic cycling may have enabled arsenic to act as a persistent,
288 structurally embedded electron donor in early microbial ecosystems. Thus, even in low-arsenic
289 environments cyanobacteria could have repeatedly faced conditions where OP was inhibited and
290 replaced by AP, limiting cumulative oxygen output.

291 Our findings show that arsenic did not merely act as a passive redox substrate in early environments,
292 but may have actively modulated the pace of oxygenation through physiological inhibition of OP.

Namely, OP may have initially inhibited itself: the oxygen it produced aggravated oxidative stress in arsenic-rich environments. However, this negative feedback may have transitioned into a positive loop, in which rising levels of oxygen ultimately promoted the widespread oxidation of both As(III) and Fe(II)[57,58]. In response to rising As(V), genomic evidence indicates a vast expansion of arsenic metabolism genes across bacteria[59]. Yet, As(V) is known to strongly sorb onto freshly precipitated Fe(III) oxides, effectively removing arsenic from the water column[17,60]. Here we show that this would have decreased arsenic-induced oxidative stress and relieved inhibition of OP, allowing photosynthetic activity – and oxygen accumulation – to increase further. Such a feedback loop may have contributed to the eventual crossing of the critical tipping point for oxygenation during the GOE.

Following the GOE, Fe(II) was largely depleted from the oceans, reducing Fe(III) oxide formation and As(V) scavenging[61]. During the mid-Proterozoic "boring billion," continental oxidative weathering, persistent anoxia and the expansion of sulfidic conditions further hindered arsenic sequestration[17,57]. Consequently, arsenic could have re-emerged as a physiological stressor, periodically constraining OP and helping maintain low oxygen levels during much of the Proterozoic.

Crucially, arsenic may have had a suppressive effect on OP itself, while simultaneously stimulating AP. This shift would have maintained high primary productivity and organic carbon burial, but without the corresponding oxygen release. By decoupling carbon burial from oxygen accumulation, this mechanism may help explain apparent discrepancies between signals for productivity and oxygen levels in the rock record after the GOE[57,62,63]. Arsenic cycling thus emerges as a potentially critical factor in modulating biogeochemical feedbacks during Earth's oxygenation, yet remains underexplored in most current models.

315 # Methods

316 **Field measurements and sampling**

317 Field measurements and sampling were conducted in Laguna Pozo Bravo (25° 30’ 58” S, 67° 34’ 42”
318 W), in the Salar de Antofalla, Argentina in late February 2019 and January 2023 at an elevation of 3330
319 m. To assess diel dynamics of oxygen and H_2S within the mat, we continuously measured depth profiles
320 of concentration on two consecutive days, in two spots of the mat. The microsensors (H_2S and Clark-
321 type O_2 with <50 µM tip width) were constructed, calibrated and used as previously described[64-67].
322 Vertical profiles were measured simultaneously by attaching the microsensors to a multi-sensor
323 holder, yielding a distance between tips of ~0.5 cm. Electricity was provided by a portable generator.
324 Using O_2 microsensor measurements, we calculated the net rates of OP as the difference in the fluxes
325 into and out of the two photosynthetically active zones.

326 In parallel with the microsensor measurements, subsamples of the mat were regularly taken for
327 porewater extraction. Cores for porewater extraction (2.5 cm inner diameter) were sampled in
328 triplicate every three hours from 1 am until 6 pm. Porewater was immediately extracted from the cores
329 (2.5 cm ID, up to 6 cm depth) at 1 cm intervals using rhizones (Rhizosphere Research Products, NL). An
330 aliquot of 500 µL porewater was instantly frozen with liquid nitrogen and stored and transported in a
331 dry shipper until arsenic speciation analysis as previously described[68]. Briefly, arsenic speciation was
332 determined by high performance liquid chromatography (HPLC; 1260 Infinity II bio inert, Agilent) using
333 a PRP-X100 column (Hamilton 5 µm, 10 mM NH_4NO_3, 10 mM $NH_4H_2PO_4$, and 500 mg/L Na_2-EDTA at a
334 flow rate of 1.0 mL/min and 25 µL injection volume) coupled to ICP-MS/MS (8900 Triple Quadrupole,
335 Agilent). Arsenic was detected in MS/MS mode using oxygen as reaction cell gas (AsO^+, m/z 75 -> 91).
336 Retention times of arsenite and arsenate were determined using individual standards. Samples
337 stabilized in 2% HNO_3 were analyzed for total As concentrations by ICP-MS/MS using Rhodium (Rh) as
338 an internal standard (AsO^+, m/z 75 -> 91; Rh^+ 103 -> 103).

339 Additional sediment cores for meta-omics (2.5 cm inner diameter, up to 4 cm depth) were sampled in
340 triplicates every three hours. The microbial mat was rapidly and carefully cut into four pieces per core
341 that were instantly frozen in liquid nitrogen for metagenomic and metatranscriptomic analyses.

342 A few additional cores were frozen intact for hyperspectral imaging. The core was sliced in half and
343 embedded with resin (EPO-TEK® MED-301-2FL) following the manufacturer's instructions. The cross
344 section of the core was then scanned using a Resonon Pika II hyperspectral camera, as described in
345 Chennu et al. (2013)[69]. Scans were used to record radiance images of 0.2 mm per pixel in 4 bands of 1
346 nm at 675, 715 and 805 nm. Reflectance images were derived by normalizing the radiance spectra of
347 all pixels to the average radiance of a standard reference board in each image.

348 Further, 10 x 5 cm pieces of mat with ~0.5 cm underlying sediment were stored in plastic containers
349 for transport and maintained in mesocosms at ~700 µmol photons m^{-2} s^{-1} underneath a water column
350 with a salinity of ~137 g L^{-1} (TropicMarine artificial saltwater), constantly circulated to maintain a
351 temperature of 21°C, until ex-situ measurements.

352 Temperature of air and water above the mat were recorded using HOBO loggers (Onset Computer
353 Corp., MA). Measurements of light intensity failed due to rapid oversaturation of the sensor signal in
354 the morning. Occasionally, pH measurements in the water column were taken using a Mettler Toledo
355 pH meter. Salinity was measured with an Atago refractometer.

356 **Assessment of diel H_2O_2 dynamics**

357 To assess the effect of light and arsenic on net O_2 production and H_2O_2 dynamics in the mat, we
358 subsampled microbial mat pieces (~ 2.5×2.5 cm) from the laboratory mesocosms and continuously
359 measured O_2 and H_2O_2 depth profiles during simulated diel light cycles, in the absence and presence
360 of dissolved arsenic. Mat pieces were cut and fixed with low-melting agarose (1%) to the bottom of
361 glass dishes. Circular flow was established with the same hypersaline water (TropicMarine artificial
362 saltwater approximately 137 g L^{-1}) used for regular maintenance of the mats, and adjusted using a
363 peristaltic pump (Minipuls 3 Abimed, Gilson). Diel cycles were simulated using halogen light sources

364 (KL 2500 and KL 1500, Schott). Microsensors (H_2O_2, and O_2 with 80-120 µM tip diameter) were
365 constructed, calibrated and used as previously described[67,70,71]. Concentration-depth profiles were
366 performed under three light conditions: dark, 500 and 1000 µmol photons m^{-2} s^{-1}. First, profiles were
367 measured without supplementing As(V), assuming that most arsenic had been washed out after four
368 months of lab maintenance. Then As(V) was added to the overlying water column to a final
369 concentration approximately 10 µM, mimicking the environmental As(V) maximum. After As(V)
370 addition, mats were left undisturbed overnight to enable the diffusion of arsenic into the mat, and diel
371 profiling began in the morning. Diel profiling was also performed in As(V)-supplemented mats after
372 addition of DCMU, an inhibitor of OP, and after autoclaving the mat as an abiotic control.

373 Depth-integrated rates of net O_2 and H_2O_2 production were calculated from the concentration depth
374 profiles by considering Fick's second law of diffusion. First, local volumetric net rates were calculated
375 as the second derivative of concentration multiplied by the diffusion coefficient corrected for
376 temperature and salinity. Volumetric depth rates were then integrated over the uppermost 5 mm of
377 the mat.

378 **Assessment of arsenic cycling rates in batch incubations**

379 To assess the dependency of light quality on arsenic cycling, small subsamples of microbial mats were
380 incubated under As(V), As(III), and LED lights targeting distinct groups of phototrophs. Hypersaline
381 water (TropicMarine artificial saltwater ~137 g L^{-1}) was deoxygenated by bubbling with helium,
382 vigorously shaking, then removing gas bubbles, repeated five times. Subsamples cut from microbial
383 mats (~200 mg) using 8 mm width cores (surface area 0.5 cm^2) were inserted into 3 mL gastight glass
384 vials with a septum cap (exetainers, Labco) which were later filled completely with deoxygenated
385 hypersaline saltwater. Then they were placed into containers on shakers, with constant flow of
386 temperature-regulated water. The incubations were subjected to 8-hour cycles of light with various
387 different spectral quality, followed by 8 hours of darkness. Controls were placed under constant
388 darkness. All light treatments were repeated with the addition of 5 µL DCMU solution (5 mM) to inhibit
389 oxygenic photosynthesis.

390 The light treatments were chosen at specific wavelengths to target different groups of phototrophs.
391 LEDs with an emission maximum (λ_{max}) at 690 nm (hexagonal high-power LEDs from Roithner
392 Lasertechnik, Vienna; Supp. Fig. S18) were used to specifically target Chl *a*, i.e., the light harvesting
393 pigment of most cyanobacteria for photosystem I and the central pigment in the reaction center of
394 both photosystems. Since an unexpected absorption maximum was found at 715 nm in the lower
395 cyanobacterial layer, we also used LEDs in the far-red range of the spectrum with λ_{max} = 715 nm to
396 target cyanobacterial Chl *f*, which can likely act as antenna in both photosystems[41,72]. Additionally, we
397 used λ_{max} = 810 to target BChl *a* of purple anoxygenic bacteria, and full-spectrum white light to target
398 all phototrophs.

399 Every three hours, three incubation vials per treatment were removed for measurements. First, oxygen
400 in each exetainer was measured with a microsensor, then 2 mL of the overlying water were filtered.
401 From the filtered water, 1 mL was fixed with 4 mL 2% zinc acetate for total dissolved sulfide
402 measurements, and 1 mL was fixed with 15.53 µL fixing solution and flash frozen for arsenic
403 measurements. Fixing solution for arsenic measurements was made by mixing 27 mL of concentrated
404 HNO_3 diluted 1:2 with ultrapure water and 100 mL fresh DTPA solution. The DTPA solution was made
405 by mixing 6.75 mL ultrapure water, 6.75 mL concentrated HNO_3 and 50 mL of 40% premade DTPA*Na_5
406 solution (Sigma Aldrich, CAS 140-01-2). Sulfide was later measured as previously described[10,73].

407 Arsenic was measured colorimetrically based on Castillejos Sepúlveda et al. (2022)[68], with
408 modifications to calculations due to the high salinity and absence of phosphate. Specifically, instead of
409 1.15 mM KIO_3, $KMnO_4$ at a final concentration of 6.9 mM was used as the oxidant to convert As(III) to
410 As(V). This is because oxidation by KIO_3 was shown to be very inefficient at high salinity. As the analysis
411 protocol from Castillejos Sepúlveda et al. (2022)[68] could also not be completely adapted for hypersaline
412 samples, we optimized the spectral analysis for the specific samples used here. The approach was
413 rigorously simplified because dissolved inorganic phosphate concentration, an interfering solute, was
414 below detection limit throughout. Absorption in the low-acidity reagent, which is proportional to both
415 As(V) and phosphate (not present) was measured at 648 nm and 760 nm. Concentration of As(V) in

416 the samples was determined based on the difference between absorption at the wavelength, i.e. the
417 spectral index, and a calibration series in the same hypersaline water. To assess the concentration of
418 As(III) absorption at the same wavelengths was determined after oxidant addition and a reaction time
419 of 3.5 h. The difference between the spectral index before and after addition was used to calculate
420 As(III) based on calibrations with As(III) standards in hypersaline water with the same composition as
421 the samples.

422 Incubations were initiated by the addition of As(V) or As(III) to enable differentiation between
423 oxidation and reduction rates. As total dissolved arsenic remained relatively constant in all incubations,
424 we calculated rates of both As(III) oxidation and As(V) reduction based only on As(V) dynamics, which
425 was favorable due to the higher accuracy of the colorimetric method for As(V)[68].

426 Given that As(V) respiration and photosynthetic As(III) oxidation likely co-occur, we conducted a
427 detailed analysis of As(V) consumption (i.e., respiration) rates to enable the calculation of
428 photosynthetic gross rates from net rates. Rates of As(V) consumption in the dark were linearly
429 dependent on As(V) concentration across the complete measured range (Fig. 4b). Assuming that As(V)
430 respiration rates were unaffected by light and solely determined by the As(V) concentration, we were
431 able to calculate light-driven gross As(III) oxidation as

432 $$G_As(III)_{oxidation} = N_As(V)_{prod} + As(V)_{resp}([As(V)]), \quad (2)$$

433 where $G_As(III)_{ox}$ is the gross rate of As(III) oxidation (i.e. gross As(V) production, Fig. 4b), $N_As(V)_{prod}$
434 is the net rate of As(V) production, (i.e. net As(III) oxidation), and $As(V)_{resp}([As(V)])$ is the rate of light-
435 independent As(V) consumption as a function of concentration derived from the linear regression in
436 Fig. 4d.

437 **Metagenomics**

438 A piece of microbial mat collected in situ at 12:30 pm, following the procedure described above, was
439 sliced into the four distinct layers (crust, green, red, brown) and sent to the Max Planck Genome Center
440 Cologne, Germany (https://mpgc.mpipz.mpg.de/home/) for processing. DNA extraction was

441 performed using the DNeasy PowerSoil Pro Kit (Qiagen). An Illumina-compatible library was prepared
442 with NEB Ultra II DNA kit (NEB) and each library was shotgun sequenced with Illumina HiSeq3000 (2 x
443 150 bp, paired-end read mode). The crust and brown layers were sequenced at a depth of 6.8 million
444 reads, while the green and red layers were sequenced at a depth of 34 million reads to target
445 cyanobacteria, which are notoriously difficult to sequence[74].

446 Raw sequences were quality-trimmed with Trimmomatic v.0.38[75], and assembled with MEGAHIT
447 v.1.2.9[76]. Initially, a co-assembly of all samples was used, but due to low cyanobacterial read depth, a
448 second assembly was prepared using only reads from the green layer of the microbial mat. Both
449 assemblies were later processed using the same workflow, but the second assembly was only used for
450 analysis of cyanobacteria.

451 Samples were mapped onto the assembly with Bowtie2 v.2.4.5[77]. Gene calling was performed with
452 Prodigal v.2.6.3[78], and the resulting gene calls were annotated in anvio v.7.1[79] using the KEGG KOfam
453 v.95.0[80] and COG v.2020[81] databases with DIAMOND v.0.9.14[82] search. Interproscan v.78[83,84] was used
454 for further annotations with the following databases: CATH-Gene3D v.4.2.0[85], CDD v.3.17[86], HAMAP
455 v.2020_01[87], PANTHER v.14.1[88], Pfam v.32.0[89], PIRSF v.3.02[90], PRINTS v.42.0[91], PROSITE Patterns and
456 PROSITE Profiles v.2019_11[92], SMART v.7.1[93], SFLD v.4[94], SUPERFAMILY v.1.75[95] and TIGRFAMs
457 v.15.0[96]. Genes related to arsenic, photosynthesis, glutaredoxins, and thioredoxins were manually
458 selected and annotated based on consensus from the automatically-generated annotations, using
459 BLASTx v.2.2.31[97] to resolve discrepancies.

460 Metagenomic analyses were initially focused on genes that could result in redox changes, before
461 binning was performed to assign genes to distinct bacterial taxa. Automatic binning was done with
462 MetaBAT2 v.2.15[98] on the large co-assembly and MaxBin2 2.2.7[99] on the second assembly. In both
463 cases, bins were manually refined in anvio. Taxonomy was assigned to bins using GTDB-TK v.95.0[100,101]
464 within anvio. The relative abundance of each bin was calculated using coverM v. 0.4.0[102] and plotted
465 using ggplot2[103] in R v. 4.0.3[104].

466 **Metatranscriptomics**

467 Microbial mat samples collected following the procedure described above in situ at 1:00 am, 9:40 am,
468 12:30 pm, 3:15 pm, and 6:30 pm were processed at the Max Planck Genome Center Cologne, Germany.
469 RNA was isolated using Quick-DNA/RNA Miniprep Plus Kit (Zymo Research). Next, an Illumina-
470 compatible library was prepared with the kit Universal Prokaryotic RNA-Seq incl. Prokaryotic
471 AnyDeplete for rRNA depletion (Tecan Genomics). Each sample was shotgun-sequenced with Illumina
472 HiSeq3000 (2x150 bp, paired-end read mode) at depths ranging from 35.5 million to 51 million reads.
473 Raw sequences were quality trimmed with Trimmomatic, then mapped onto the metagenomic
474 assemblies with BBmap v38.73[105], and used featureCounts from Rsubread v. 1.22.2 to obtain counts
475 of each gene per metatranscriptomic sample. To compare gene transcription across samples, counts
476 of each gene call were normalized by calculating Transcripts Per Million (TPM) as previously
477 described[106]. The TPM of all gene calls annotated with the same function (i.e.- the same gene name)
478 were summed, and used to make heatmaps with Pheatmap v.1.0.12[107] in R.

479 Data availability

480 Data has been submitted to the EMBL Nucleotide Sequence Database (ENA). Metagenomic and
481 metatranscriptomic raw reads, as well as cyanobacterial metagenome-assembled genomes can be
482 found under project number PRJEB41764. Metagenome-assembled genomes from the co-assembly
483 can be found under project number PRJEB73824.

484 Figures

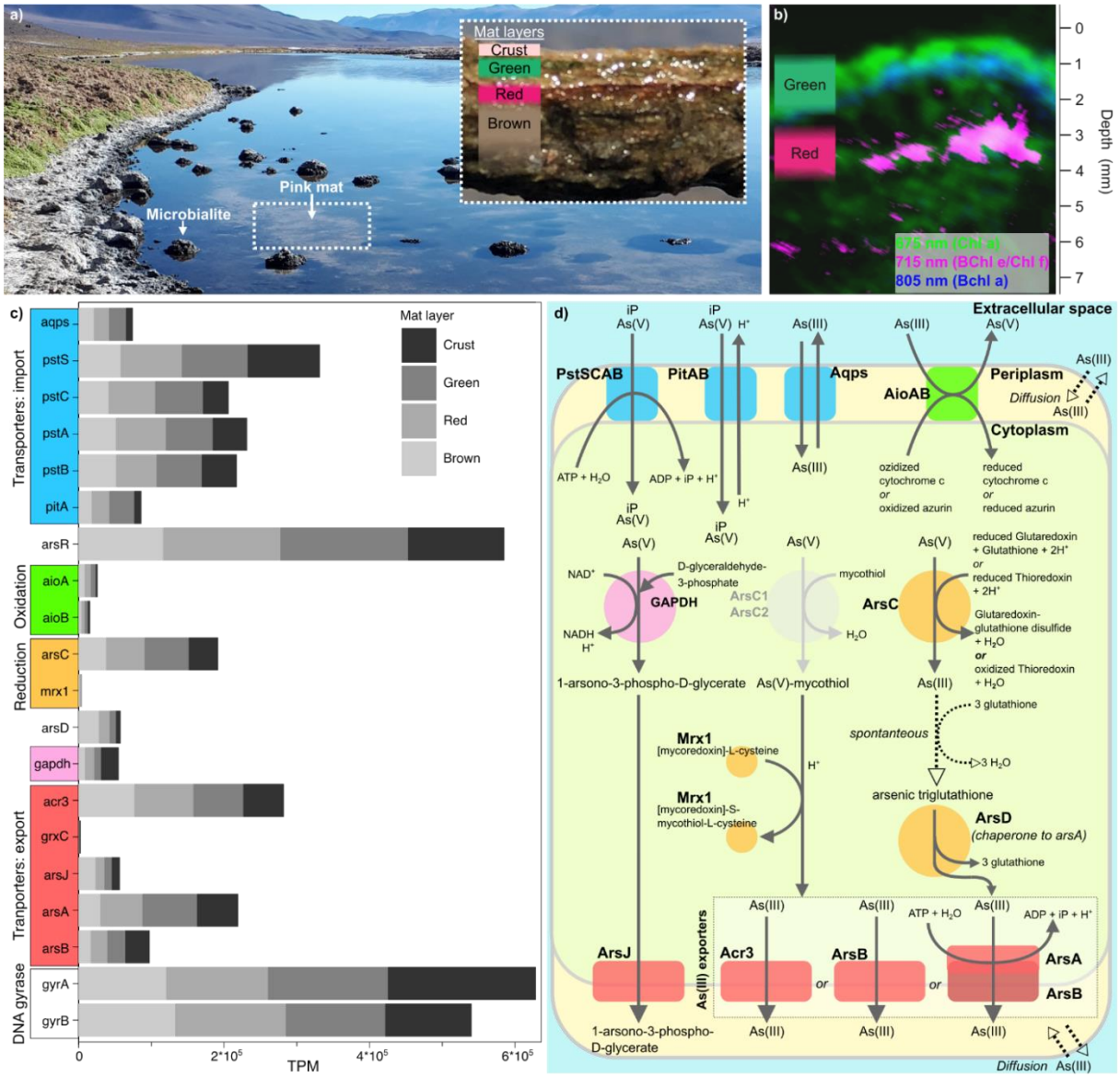

485

486 **Figure 1. The microbial mats of Laguna Pozo Bravo.** a) Microbialites and microbial mats (pink and
487 lithifying gray) found in Pozo Bravo. Inset is a pink microbial mat cross section, with layers indicated.
488 b) Distribution of selected pigments in the top 7 mm of Pozo Bravo microbial mat, captured by
489 hyperspectral imaging, based on the second derivative of reflectance spectra around 675 nm, 715 nm,
490 and 805 nm as indicated by different colors. Pigments with the corresponding in-vivo absorption
491 maxima at the respective wavelength are shown in parentheses. c) Presence of genes associated with
492 arsenic cycling and housekeeping genes (DNA gyrase (*gyrA*, *gyrB*)) in the metagenome of Pozo Bravo
493 microbial mat. Shades of gray represent the number of gene copies (normalized as Transcripts Per
494 Million, TPM[106]) from each microbial mat layer that were mapped to the metagenomic assembly, which
495 was made using reads from all microbial mat layers. Almost as many gene copies are dedicated to
496 arsenic cycling as for housekeeping tasks, suggesting intense metabolizing of arsenic species. d)

497 Overview on the pathways of redox arsenic transformation detected in Pozo Bravo mats, based on
498 previously reported functions of arsenic genes[20,108-110]. Genes were broadly classified in expressing
499 transporters for arsenic uptake (blue) and export (red), enzymes involved in reduction of As(V)
500 (orange), oxidation of As(III) (green), and production and export of organic arsenicals (pink). ArsC1 and
501 ArsC2 are shown in gray since their presence could not be determined in the metagenome). Details
502 and a list of abbreviations can be found in Table S1 and in the supplementary results Table 3.

503

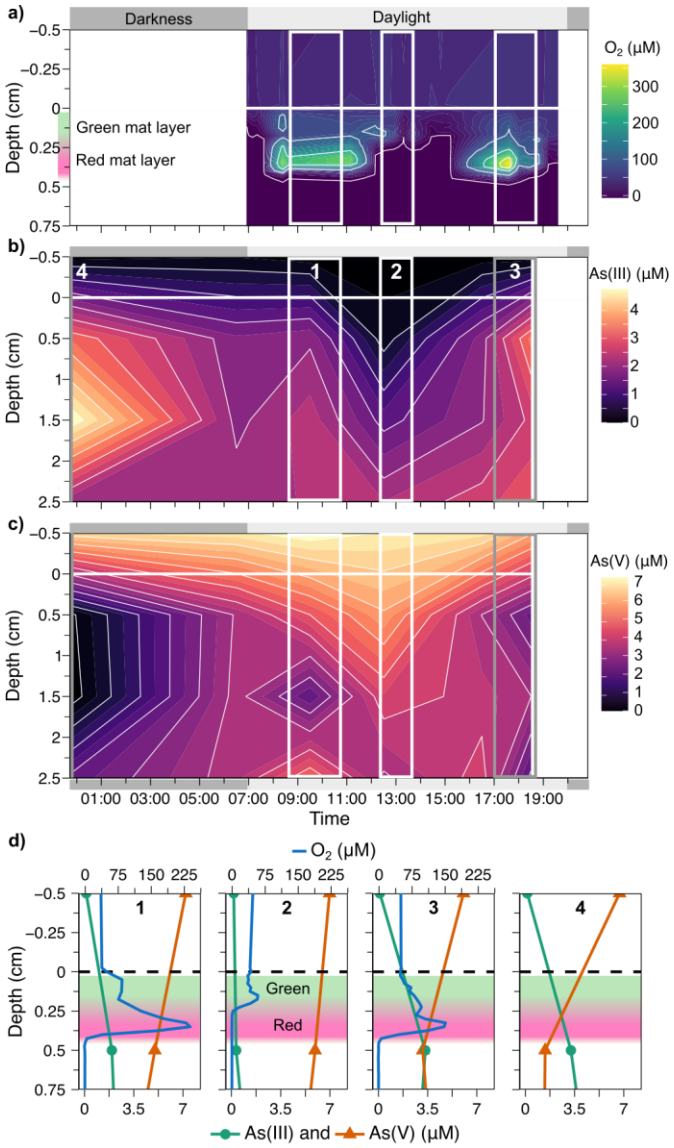

Figure 2. Diel dynamics of O_2 production and arsenic speciation within the mats. Depth profiles of dissolved oxygen (a), and speciation of inorganic arsenic over a diel cycle in porewater from Pozo Bravo (b & c, n=1-3 per depth). The microbial mat surface is at 0 cm depth (horizontal white line in a)-c), black dotted line in d)). Profiles selected from various points in time are shown in d). The timepoints used for d) are indicated by rectangles in a)-c), following the numbering in b). Profile 4 represents a single point in time (00:30). Colored background represents the estimated placement of the green and red microbial mat layers (Fig. 1b). The chosen profiles exemplify the oxygen production during the morning (d1) and late afternoon (d3), with a period of interruption in between (d2). D4 shows a comparison of the dissolved arsenic speciation at night (00:30). The interruption in oxygen production coincides with a maximum in dissolved As(V). Net volumetric rates calculated based on the concentration depth profiles of oxygen measured in two replicate spots can be found in Extended data Fig. 3a, and depth integrated rates over a diel cycle in Extended data Fig. S3b.

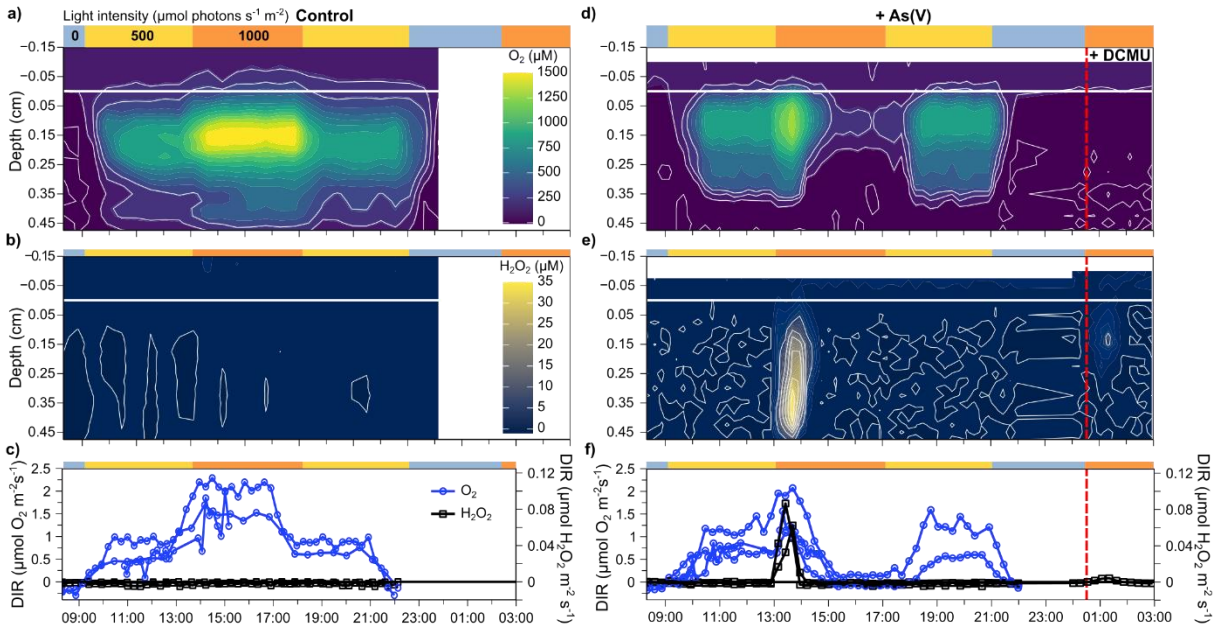

Figure 3. As(V) inhibits OP at high light and induces H_2O_2 evolution. O_2 and H_2O_2 measurements of microbial mats before (a-c) and after As(V) addition (10 µM final concentration) (d-f)). Bars over each graph represent light conditions over time, as either darkness, low light (500 µmol photons m^{-2} s^{-1}), or high light (1000 µmol photons m^{-2} s^{-1}). Contour plots show concentration of O_2 (a,d) or H_2O_2 (c,e) across the depth of the microbial mat over time. The solid white horizontal line represents the mat surface at depth 0. The vertical dashed line in d-f indicates time of DCMU addition, an inhibitor of oxygenic photosynthesis. c) and f) Depth-integrated rates of production (DIR) for O_2 (n=3 pieces of mat) and H_2O_2 (n=2 pieces of mat).

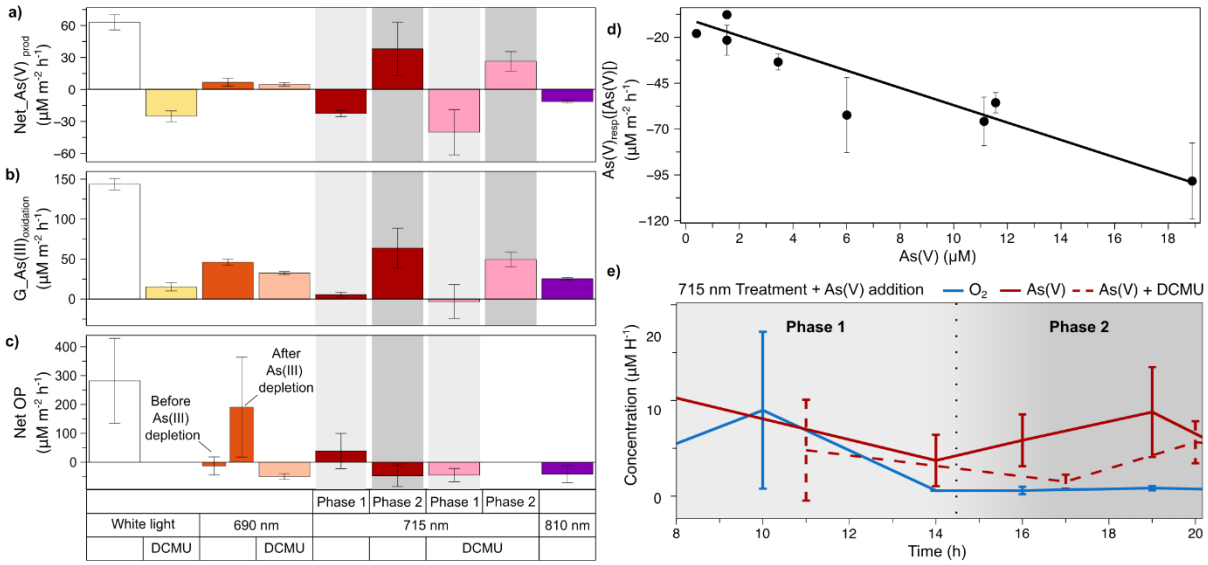

Figure 4. Rates of arsenic cycling dependent on light quality and photosynthesis. a) Net rates of As(V) production ($Net_As(V)_{prod}$) in incubations of mat slurries with and without DCMU, under white light, light at λmax = 690 nm to target Chl *a*, λmax = 715 nm to target Chl *f*, and light at λ_{max} =810 nm to target BChl *a*. The gray bars overlaid in 715 nm represent phase 1 and phase 2 of As(V) production, as shown in (e). b) Rate of As(V) consumption, i.e. As(V) respiration, in the dark dependent on the concentration of As(V). c) Gross rates of As(III) oxidation ($G_As(III)_{oxidation}$) calculated from (a) by adding the expected rate of As(V) removal ($As(V)_{resp}([As(V)])$) from (b) according to Eq (1). d) Net rates of oxygenic photosynthesis in the same incubations as in (a) and (c). In e) an example for a time series of dissolved As(V) and O_2 in batch incubations is shown, based on which the net rates of arsenic production in (a) and net OP in (d) were calculated. The slurry was initially exposed to ~20 µM As(V) and, after a dark phase, exposed to light of λmax = 715 nm. Errors represent the standard deviation of concentration in separate vials (n=3). In phase 1, which represents the initial hours of exposure to light, net O_2 production occurred and arsenite was not photosynthetically oxidized. In phase 2, after sustained exposure to light, O_2 production ceased and As(III) was photosynthetically oxidized to As(V). A similar pattern was observed in the treatment with DCMU, which blocks OP. Namely, As(V) was reduced for an initial five hours (phase 1), after which As(III) was photosynthetically oxidized to As(V) (phase 2).

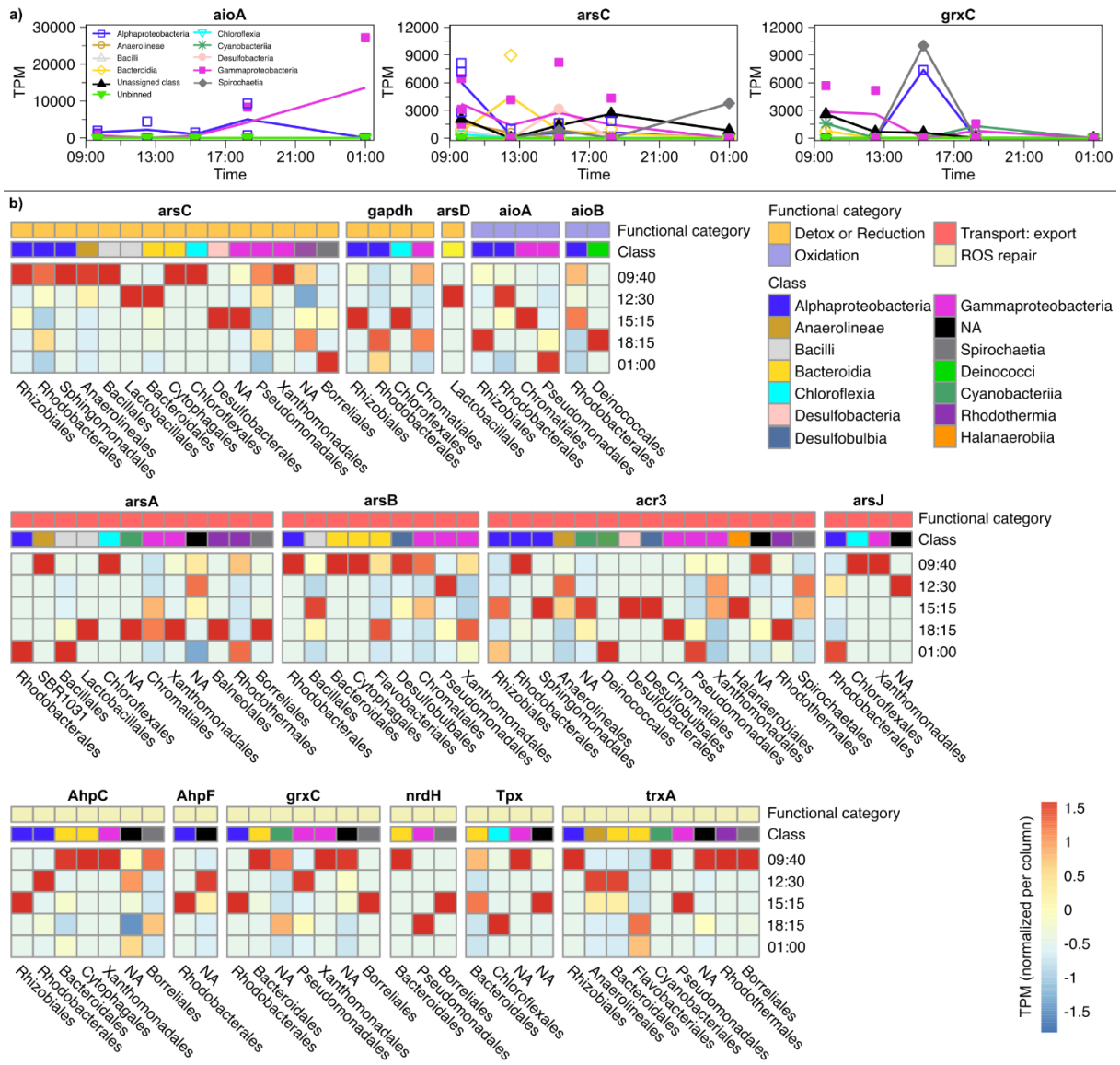

Figure 5. Transcriptional activity of arsenic-related genes across the Pozo Bravo microbial mat and selected taxa. a) Sum of *aioA*, *arsC*, and *grxC* transcription, in TPM, over the metatranscriptome of all layers of Pozo Bravo microbial mat. *aioA* is involved in arsenite oxidation, *arsC* is involved in arsenate reduction, and *grxC* may be part of arsenate reduction or reactive oxygen species response pathways. b) Transcription of genes related to arsenic cycling in selected taxa, shown as the sum of TPM per gene, normalized across all timepoints (i.e., per column). Normalization was performed due to the varying number of gene copies found per gene. Higher gene transcription is represented in red, lower transcription in blue. Transcription of *pufL* and *pufM*, which encode for photosynthetic reaction center II, can be found in the Supplementary Results (Fig. S2). An overview of transcription of genes in cyanobacterial bins can be found in Extended data Fig. 7.

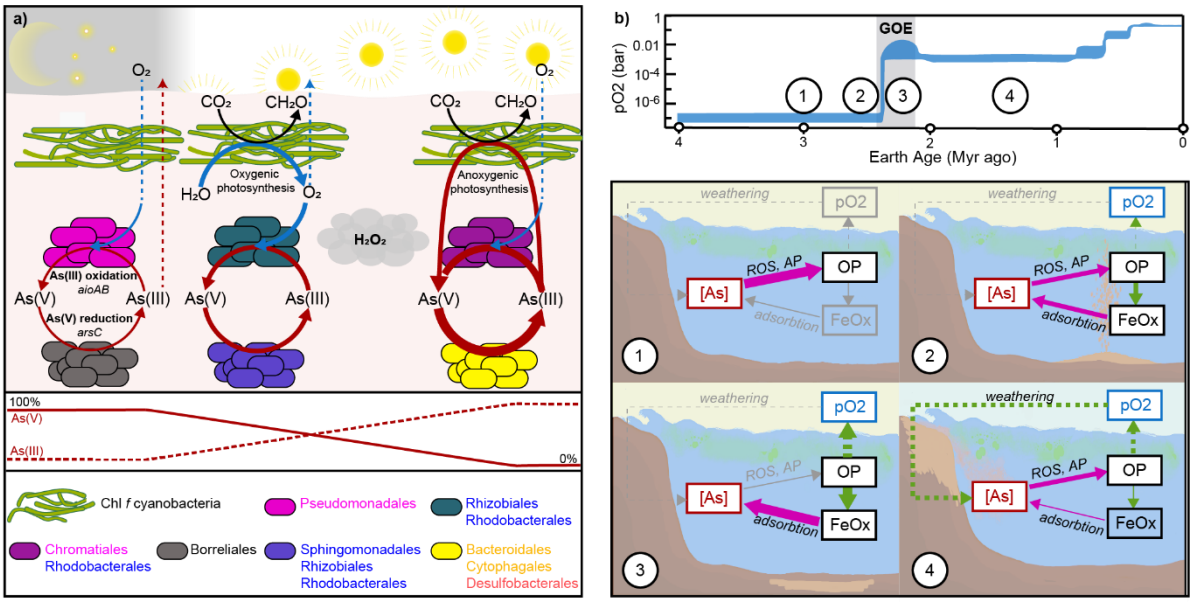

Figure 6. Proposed metabolic activities driving arsenic cycling through a diel cycle in the layers of Pozo Bravo microbial mats (a) and hypothesized feedback mechanisms between arsenic cycling and oxygenic photosynthesis in the Precambrian ocean (b). The mat model in (a) is based on pooling insights from hyperspectral imaging, process rate measurements and metatranscriptomic analyses. ROS production during the morning, afternoon and late afternoon is indicated with grey clouds. The conceptual model in (b) links these physiological responses to possible feedback mechanisms in the ancient ocean, with four numbered stages corresponding to the timeframes in the upper panel depicting Earth's oxygenation history. 1. High As and ROS: OP is suppressed and cyanobacteria shift to AP, lowering net oxygen production. 2. OP recovery: Fe(II) oxidation by the photosynthetically produced oxygen yields Fe(III), which removes As(V) from the water column. 3. Low As and OP dominance: Reduced arsenic stress enables sustained OP and higher oxygen output. 4. Oxidative weathering: reintroduces As to oceans, reinstating OP suppression and tempering oxygen levels. Green arrows indicate enhancing effects, magenta arrows negative effects. Solid arrows: processes within the photic zone; dashed arrows: global-scale processes operating over geological timescales.

572 Extended Data Figures

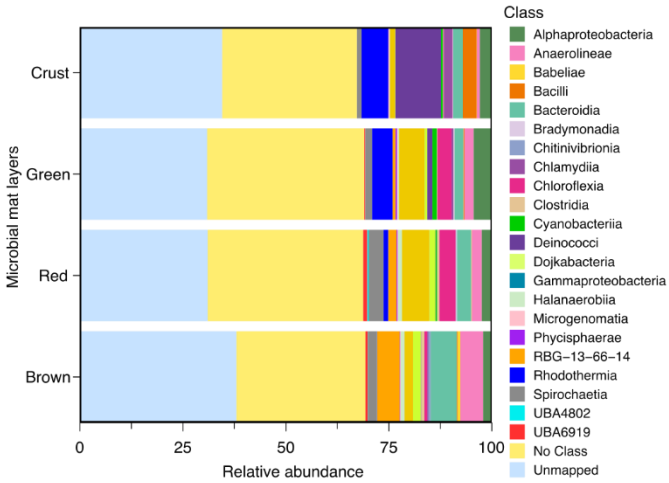

573

574 **Extended data Figure 1.** Taxonomic profile of phyla from metagenomic bins in a Pozo Bravo microbial
575 mat. The bins were selected from a metagenomic assembly made using reads from all vertically-
576 stratified layers (crust, green, red, brown). Only bins with over 55% completeness and less than 10%
577 redundancy are shown (Supplementary Table S1). Relative abundance was obtained by mapping the
578 reads from each individual layer metagenome to the total set of bins. Results were summarised by
579 grouping bins by phylum.

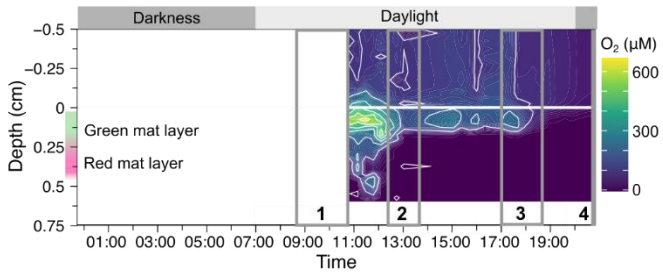

580

581 **Extended data Figure 2.** Depth profiles of dissolved oxygen in Pozo Bravo microbial mat, replicate of
582 Fig. 2a and corresponding to "mat b" in Extended data Fig. 3. The microsensor profiles shown in
583 Extended data Fig. 3 were selected from times (1-4), as shown by the gray boxes with black numbers.

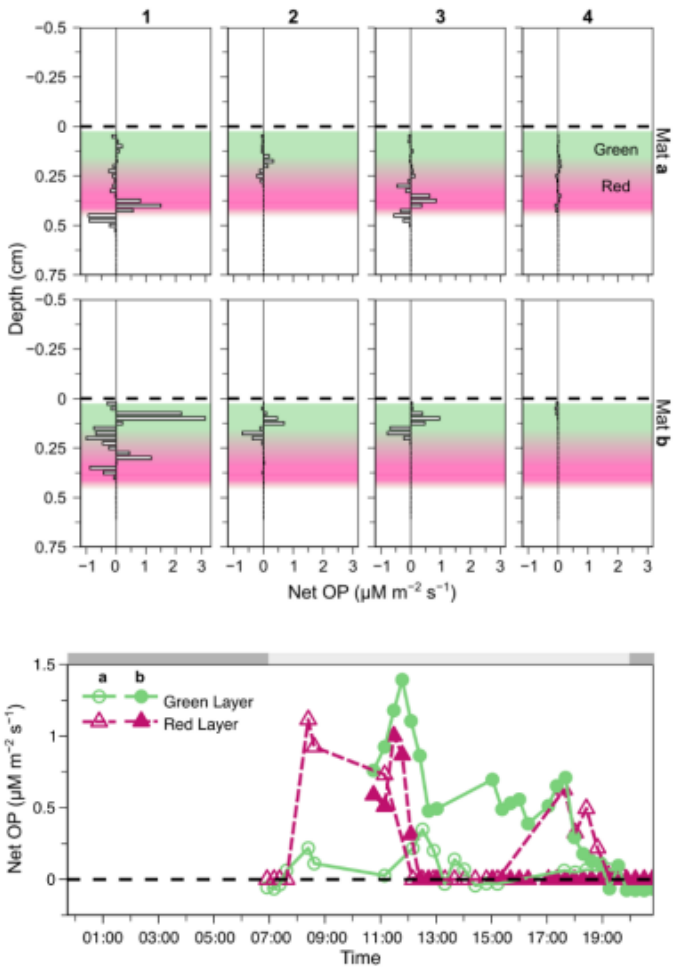

Extended data Figure 3. Net volumetric rates of oxygenic photosynthesis. In a), examples for local volumetric rates are shown through depth, calculated from the oxygen profiles shown in Extended data Fig 2 and in Fig. 2a in the main text, at the times specified by 1-4 in Fig 2. Colored bars indicate the estimated location of the green and red microbial mat layers. In b), the corresponding depth-integrated rates of net OP over a diel cycle in the green and red layers are shown.

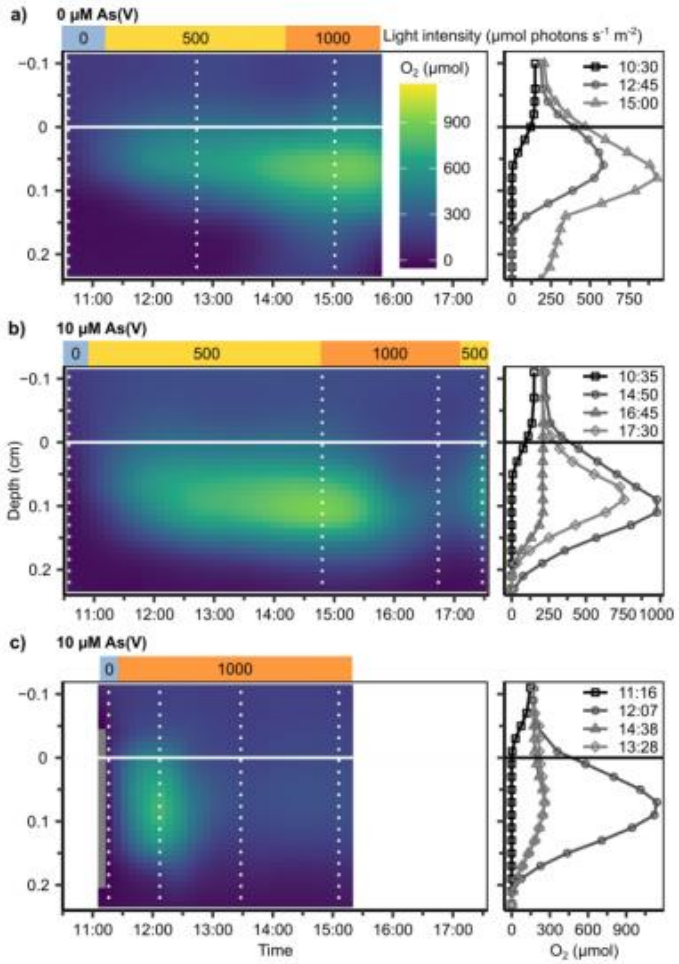

Extended data Fig. 4. Microsensor measurements of Pozo Bravo microbial mat incubations under two light conditions (500 and 1000 µmol photons m-2 s-1), with and without 10 µM As(V) addition. Selected profiles, indicated by vertical dotted lines, are shown on the right panels. Microbial mat surface is indicated by horizontal lines at depth 0. a) and b) were obtained from the same piece of microbial mat, while c) was measured in a separate mat sample.

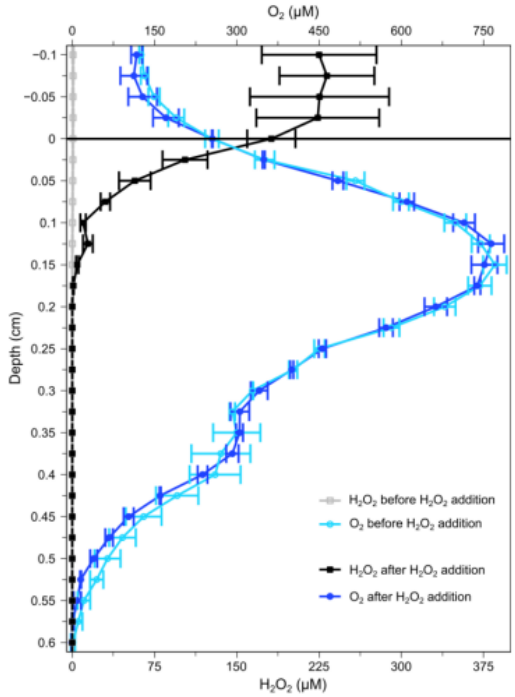

Extended data Figure 5. Ex situ H_2O_2 and O_2 microsensor depth profiles of Pozo Bravo microbial mat, taken before and after the addition of H_2O_2 to the water column (n=3).

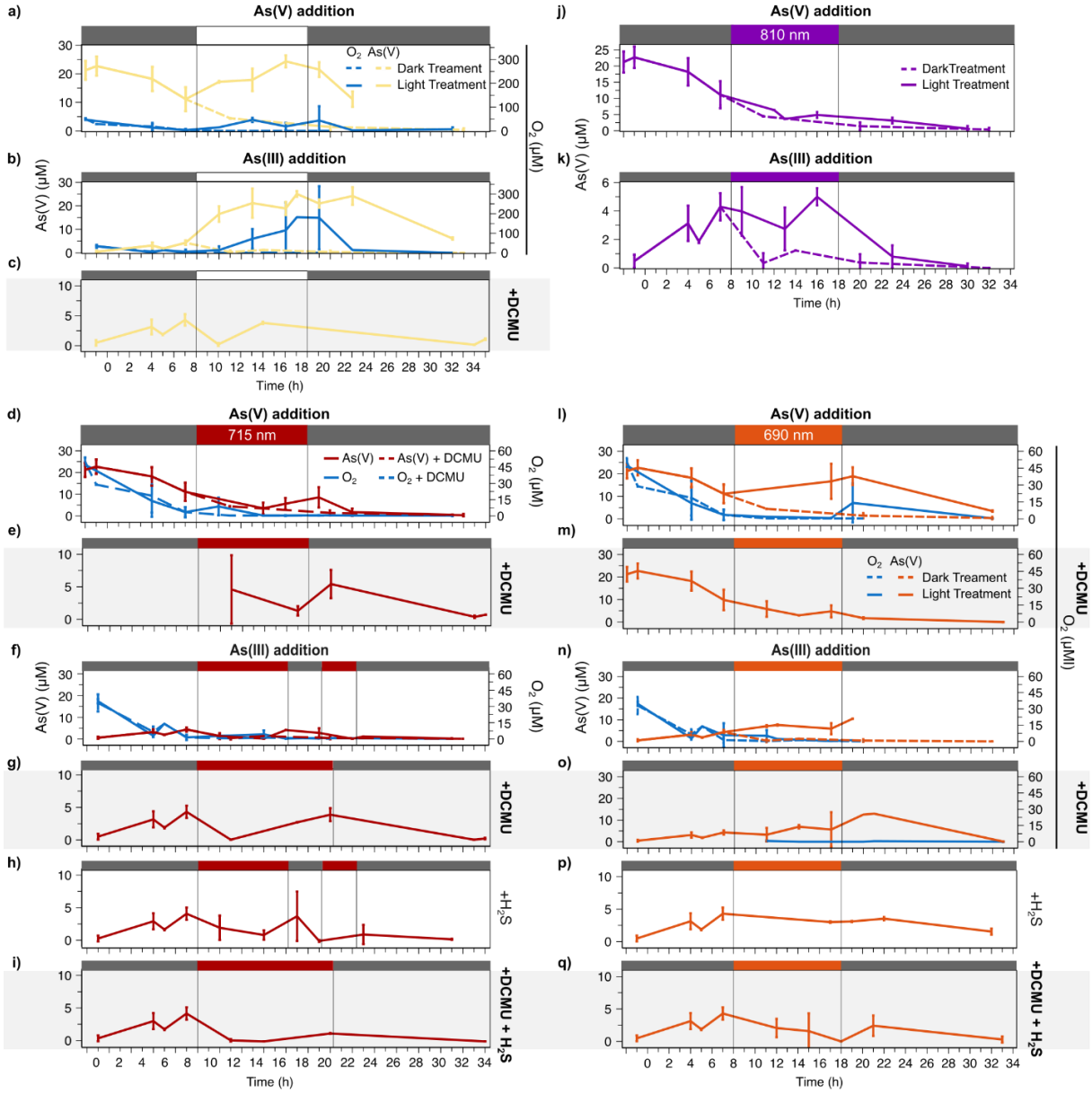

Extended data Fig. 6. Time series of dissolved As(V) and O_2 in the overlying water of Pozo Bravo microbial mat incubations, with or without DCMU, an oxygenic photosynthesis inhibitor, treated with white light targetting all phototrophs (a-c), light at 715 nm targetting photosystem I (d-i), light at 810 nm targetting photosystem II (j, k) and light at 690 nm targetting cyanobacterial chl a (l-q). Periods of light are indicated by the colored bars at the top of each graph (white = white light, red = light at 715 nm, purple = light at 810 nm, orange = light at 690 nm). Dark gray bars at the top of the graphs represent periods of darkness. In the As(III) addition experiment at 710 nm light (f and h), incubations without DCMU addition were treated with an extra period of darkness in the afternoon, while in the treatment with DCMU lights were kept on for the entire daylight period. Error bars represent standard deviation, n=3. As(III), As(V), and H_2S were added to a final concentration of 10 µM.

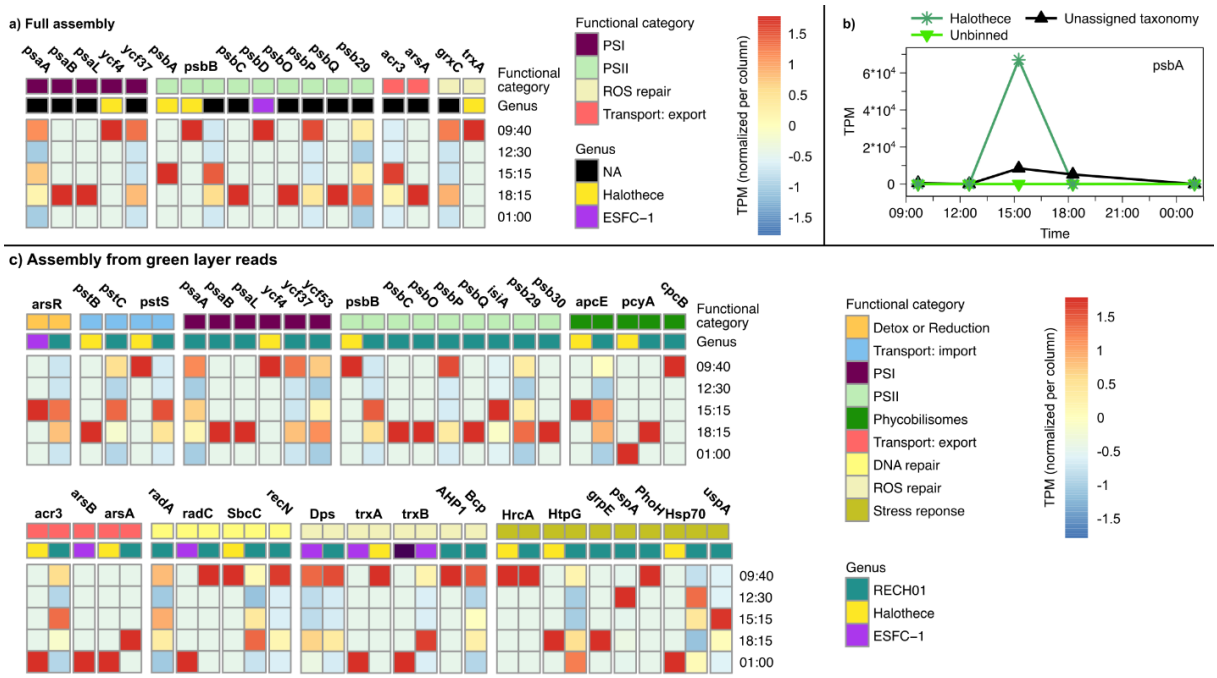

Extended data Figure 7: Gene expression, as TPM normalized per column, in bins of order Cyanobacteriia related to arsenic, photosynthesis, DNA repair, and responses to reactive oxygen species (ROS), as well as heat, salinity, and temperature stress responses in a Pozo Bravo microbial mat. In (a) and (c) heatmaps are shown, with higher gene expression in red, lower expression in blue. Normalization was performed due to the varying number of gene copies found per gene. TPM was calculated from metatranscriptomic reads mapped to the metagenome assembly made using only reads from the green microbial mat layer to specifically target cyanobacteria. Two assemblies were made because only a few cyanobacterial genes were found when all samples were used to make the assembly (a), but more cyanobacterial genes could be recovered after the assembly of only the green Pozo Bravo layer (b). In (b) expression of gene psbA, shown as the sum of TPM per genus, is shown. TPM was calculated from metatranscriptomic reads mapped to a metagenomic assembly made from reads of all layers of Pozo Bravo microbial mat. Reads labelled as 'unassigned taxonomy' originate from two separate bins to which no taxonomic information could be assigned.

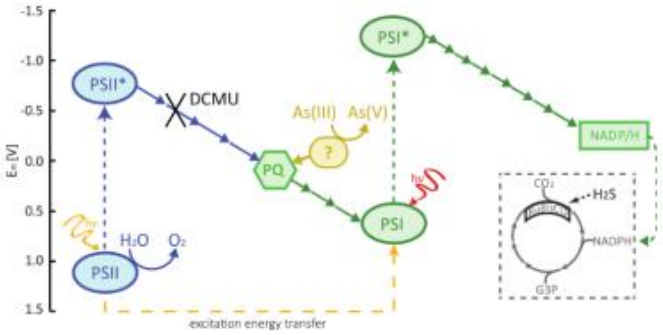

Extended data Figure 8: Schematic view of the electron transport during cyanobacterial photosynthesis, indicating where DCMU interrupts electron flow, thus blocking oxygenic photosynthesis. The point of entry for electrons from As(III) must thus be after PSII and only involve PSI (PS= photosystem, PQ= plastoquinone, ?= hypothetical enzyme). Modified from [3].

Acknowledgements

We would like to thank Secretaría de Medio Ambiente de la Provincia de Catamarca for providing the research permit (Expte.EX-2022-02222431-CAT-DPB#SEAS), and Secretaría de Política Ambiental en Recursos Naturales, Ministerio de Ambiente y Desarrollo Sostenible de la Nación Argentina for providing the certificate of compliance (Title: IF-2023-65966642-APN-SPARN#MAD, UId: ABSCH-IRCC-AR-264943-1) and the export certificate for genetic resources (CE-2023-69835755-APN-SPARN#MAD). We would like to express our gratitude to Luis Ahumada for his assistance during the field campaigns, and the native communities of Antofalla, El Peñón, and Antofagasta de la Sierra for their valuable support. We the Max Planck-Genome-centre Cologne (http://mpgc.mpipz.mpg.de/home/) for performing DNA and RNA extractions and sequencing, in this study. We are thankful to Gert Bange, Pieter Visscher, Christophe Dupraz, Pascal Philippot and Brendan Burns for fruitful discussions. The authors also thank the laboratory technicians in the Microsensor working group, the mechanical workshop in MPI Bremen, David Benito Merino, Marit van Erk, Britta Planer-Friedrich, Martina Alisch, and Boran Kartal for their help with labwork, advice, and laboratory equipment.

Author contributions

J.M.K. and A.C.S. conceptualized the study. J.M.K. supervised the project. A.C.S. and J.M.K. led the experiments and wrote the first draft. Incubation experiments were designed and performed by A.C.S., J.M.K., W.M., and E.M. Ex-situ microsensor measurements were conducted by K.S. and J.M.K. Arsenic speciation analyses were carried out by C.K., J.M.K., and A.C.S. Meta-omics analyses were performed by D.R.S., F.A.V., and A.C.S. A.C. conducted hyperspectral imaging. Fieldwork was carried out by A.C.S., J.M.K., D.D-W., F.A.V., E.M., and M.E.F. Figures were prepared by A.C.S., J.M.K., and D.D-W. Resources and materials were provided by M.E.F., D.d.B., and J.M.K. All authors contributed to and approved the final manuscript.

Competing interests

The authors declare no competing interests.

References

1 Lenton, T. M. & Daines, S. J. Matworld - the biogeochemical effects of early life on land. *New Phytologist*, doi:10.1111/nph.14338 (2016).

2 Lalonde, S. V. & Konhauser, K. O. Benthic perspective on Earth's oldest evidence for oxygenic photosynthesis. *Proceedings of the National Academy of Sciences of the United States of America* **112**, 995-1000, doi:10.1073/pnas.1415718112 (2015).

3 Dick, G. J., Grim, S. L. & Klatt, J. M. Controls on O_2 Production in Cyanobacterial Mats and Implications for Earth's Oxygenation. *Annual Review of Earth and Planetary Sciences* **46**, 123-147, doi:10.1146/annurev-earth-082517-010035 (2018).

4 Nisbet, E. G. & Fowler, C. M. R. in *Treatise on Geochemistry* Vol. 8-9 1-39 (Elsevier, 2003).

5 Sleep, N. H. The Hadean-Archaean Environment. *Cold Spring Harbor Perspectives in Biology* **2**, a002527-a002527, doi:10.1101/cshperspect.a002527 (2010).

6 Johnston, D. T., Wolfe-Simon, F., Pearson, A. & Knoll, A. H. Anoxygenic photosynthesis modulated Proterozoic oxygen and sustained Earth's middle age. *Proceedings of the National Academy of Sciences of the United States of America* **106**, 16925-16929, doi:10.1073/pnas.0909248106 (2009).

7 Olejarz, J., Iwasa, Y., Knoll, A. H. & Nowak, M. A. The Great Oxygenation Event as a consequence of ecological dynamics modulated by planetary change. *Nature Communications 2021 12:1* **12**, 1-9, doi:10.1038/s41467-021-23286-7 (2021).

8 Ozaki, K., Thompson, K. J., Simister, R. L., Crowe, S. A. & Reinhard, C. T. Anoxygenic photosynthesis and the delayed oxygenation of Earth's atmosphere. *Nature Communications* **10**, 1-10, doi:10.1038/s41467-019-10872-z (2019).

9 Cohen, Y., Padan, E. & Shilo, M. Facultative anoxygenic photosynthesis in the cyanobacterium *Oscillatoria limnetica*. *Journal of bacteriology* **123**, 855-861 (1975).

10 Klatt, J. M. *et al.* Anoxygenic photosynthesis controls oxygenic photosynthesis in a cyanobacterium from a sulfidic spring. *Applied and environmental microbiology* **81**, 2025-2031, doi:10.1128/AEM.03579-14 (2015).

11 Grim, S. L. & Dick, G. Photosynthetic versatility in the genome of Geitlerinema sp. PCC 9228 (formerly Oscillatoria limnetica 'Solar Lake'), a model anoxygenic photosynthetic cyanobacterium. *Frontiers in Microbiology* **7**, 1546-1546, doi:10.3389/fmicb.2016.01546 (2016).

12 Cohen, Y., Jørgensen, B. B., Revsbech, N. P. & Poplawski, R. Adaptation to hydrogen sulfide of oxygenic and anoxygenic photosynthesis among cyanobacteria. *Applied and environmental microbiology* **51**, 398-407 (1986).

13 Kelly, D. J. & Dow, C. S. *Microbial Photosynthesis*. Vol. 1 (Springer Singapore, 2020).

14 de Beer, D., Meyer, V., Klatt, J. & Li, T. Photosynthesis under very high oxygen concentrations in dense microbial mats and biofilms. *bioRxiv*, 335299, doi:10.1101/335299 (2018).

15 Hamilton, T. L., Klatt, J. M., de Beer, D. & Macalady, J. L. Cyanobacterial photosynthesis under sulfidic conditions: Insights from the isolate Leptolyngbya sp. strain hensonii. *ISME Journal* **12**, 568-584, doi:10.1038/ismej.2017.193 (2018).

16 Martin, W. F., Bryant, D. A. & Beatty, J. T. A physiological perspective on the origin and evolution of photosynthesis. *FEMS Microbiology Reviews* **42**, 205-231, doi:10.1093/femsre/fux056 (2018).

17 Smedley, P. L. & Kinniburgh, D. G. A review of the source, behaviour and distribution of arsenic in natural waters. *Applied Geochemistry* **17**, 517-568, doi:10.1016/S0883-2927(02)00018-5 (2002).

18 Oremland, R. S., Saltikov, C. W., Wolfe-Simon, F. & Stolz, J. F. Arsenic in the evolution of earth and extraterrestrial ecosystems. *Geomicrobiology Journal* **26**, 522-536, doi:10.1080/01490450903102525 (2009).

19 Kulp, T. R. *et al.* Arsenic(III) fuels anoxygenic photosynthesis in hot spring biofilms from Mono Lake, California. *Science* **321**, 967-970, doi:10.1126/SCIENCE.1160799 (2008).

20 Slyemi, D. & Bonnefoy, V. How prokaryotes deal with arsenic. *Environmental Microbiology Reports* **4**, 571-586, doi:10.1111/j.1758-2229.2011.00300.x (2012).

21 Nagy, C. I. *et al.* Coregulated genes link sulfide: Quinone oxidoreductase and arsenic metabolism in Synechocystis sp. strain PCC6803. *Journal of Bacteriology* **196**, 3430-3440, doi:10.1128/JB.01864-14 (2014).

22 Visscher, P. T. *et al.* Modern arsenotrophic microbial mats provide an analogue for life in th e anoxic Archean. *Communications Earth & Environment* **1**, 1-10, doi:10.1038/s43247-020-00025-2 (2020).

23 Rascovan, N., Maldonado, J., Vazquez, M. P. & Eugenia Farías, M. Metagenomic study of red biofilms from Diamante Lake reveals ancient a rsenic bioenergetics in haloarchaea. *The ISME Journal* **10**, 299-309, doi:10.1038/ismej.2015.109 (2016).

24 Sancho-Tomás, M. *et al.* Distribution, redox state and (bio)geochemical implications of arsenic in present day microbialites of Laguna Brava, Salar de Atacama. *Chemical Geology* **490**, 13-21, doi:10.1016/j.chemgeo.2018.04.029 (2018).

25 Sancho-Tomás, M. *et al.* Geochemical evidence for arsenic cycling in living microbialites of a High Altitude Andean Lake (Laguna Diamante, Argentina). *Chemical Geology* **549**, 119681, doi:10.1016/j.chemgeo.2020.119681 (2020).

26 Kurth, D. *et al.* Arsenic metabolism in high altitude modern stromatolites revealed by metagenomic analysis. *Scientific Reports* **7**, 1024, doi:10.1038/s41598-017-00896-0 (2017).

27 Vignale, F. A. *et al.* Lithifying and Non-Lithifying Microbial Ecosystems in the Wetlands and Salt Flats of the Central Andes. *Microbial Ecology* **83**, 1-17, doi:10.1007/s00248-021-01725-8 (2022).

28 Vignale, F. A. *et al.* Seasonal biogeochemical variations in a modern microbialite reef under early Earth-like conditions. *bioRxiv*, 2025.2002.2022.639630, doi:10.1101/2025.02.22.639630 (2025).

29 Lencina, A. I., Soria, M. N., Gomez, F. J., Gérard, E. & Farias, M. E. Composite microbialites: Thrombolite, dendrolite, and stromatolite ass ociations in a modern environment, Pozo Bravo lake, Salar de Antofalla , Catamarca Puna, Argentina. *Journal of Sedimentary Research* **91**, 1305-1330, doi:10.2110/jsr.2020.166 (2021).

30 Nisbet, E. G. & Fowler, C. M. R. Archaean metabolic evolution of microbial mats. *Proceedings of the Royal Society B: Biological Sciences* **266**, 2375-2382, doi:10.1098/rspb.1999.0934 (1999).

31 Stomp, M., Huisman, J., Stal, L. J. & Matthijs, H. C. P. Colorful niches of phototrophic microorganisms shaped by vibrations of the water molecule. *The ISME Journal* **1**, 271-282, doi:10.1038/ismej.2007.59 (2007).

32 Yacobi, Y. Z., Köhler, J., Leunert, F. & Gitelson, A. Phycocyanin-specific absorption coefficient: Eliminating the effect of chlorophylls absorption. *Limnology and Oceanography: Methods* **13**, 157-168, doi:10.1002/lom3.10015 (2015).

33 Jørgensen, B. B. *et al.* Photosynthetic action spectra and adaptation to spectral light distribution in a benthic cyanobacterial mat. *Applied and Environmental Microbiology* **53**, 879-886, doi:10.4319/lo.1992.37.8.1813 (1987).

34 Miller, L. C. *et al.* Composition, Organisation and Function of Purple Photosynthetic Machinery. *Microbial Photosynthesis*, 73-114, doi:10.1007/978-981-15-3110-1_4 (2020).

35 Blankenship, R. E., Olson, J. M. & Miller, M. in *Anoxygenic Photosynthetic Bacteria* 399-435 (Kluwer Academic Publishers, 1995).

36 Sawicki, A., Chen, M., Sawicki, A. & Chen, M. Molecular Mechanism of Photosynthesis Driven by Red-Shifted Chlorophylls. *Microbial Photosynthesis*, 3-42, doi:10.1007/978-981-15-3110-1_1 (2020).

37 Hoeft McCann, S. *et al.* Arsenite as an Electron Donor for Anoxygenic Photosynthesis: Description of Three Strains of Ectothiorhodospira from Mono Lake, California and Big Soda Lake, Nevada. *Life* **7**, 1, doi:10.3390/life7010001 (2016).

38 Averina, S., Velichko, N., Senatskaya, E. & Pinevich, A. Far-red light photoadaptations in aquatic cyanobacteria. *Hydrobiologia* **813**, 1-17, doi:10.1007/s10750-018-3519-x (2018).

39 Gan, F. & Bryant, D. A. Adaptive and acclimative responses of cyanobacteria to far-red light. *Environmental Microbiology* **17**, 3450-3465, doi:10.1111/1462-2920.12992 (2015).

40 Gan, F., Shen, G. & Bryant, D. A. Occurrence of far-red light photoacclimation (FaRLiP) in diverse cyano bacteria. *Life* **5**, 4-24, doi:10.3390/life5010004 (2015).

41 Gisriel, C. J. *et al.* Structure of a monomeric photosystem II core complex from a cyanobacterium acclimated to far-red light reveals the functions of chlorophylls d and f. *Journal of Biological Chemistry* **298**, 101424, doi:10.1016/J.JBC.2021.101424/ATTACHMENT/E0177B24-B0ED-4877-814E-AD8491135B45/MMC2.ZIP (2022).

42 Antonaru, L. A. *et al.* Evolution of far-red light photoacclimation in cyanobacteria. *Current Biology* **35**, 2539-2553.e2534, doi:10.1016/j.cub.2025.04.038 (2025).

43 Flores-Kim, J. & Darwin, A. J. The Phage Shock Protein Response. *Annual review of microbiology* **70**, 83-101, doi:10.1146/ANNUREV-MICRO-102215-095359 (2016).

44 Junglas, B. *et al.* PspA adopts an ESCRT-III-like fold and remodels bacterial membranes. *Cell* **184**, 3674-3688.e3618, doi:10.1016/J.CELL.2021.05.042 (2021).

45 Blokhina, O., Virolainen, E. & Fagerstedt, K. Antioxidants, oxidative damage and oxygen deprivation stress: A review. *Annals of Botany* **91**, 179-194, doi:10.1093/aob/mcf118 (2003).

46 Dmitrieva, V. A., Tyutereva, E. V. & Voitsekhovskaja, O. V. Singlet Oxygen in Plants: Generation, Detection, and Signaling Roles. *Int J Mol Sci* **21**, doi:10.3390/ijms21093237 (2020).

47 Razo, L. M. *et al.* Stress proteins induced by arsenic. *Toxicology and Applied Pharmacology* **177**, 132-148, doi:10.1006/TAAP.2001.9291 (2001).

48 Fu, H. L., Rosen, B. P. & Bhattacharjee, H. Biochemical characterization of a novel ArsA ATPase complex from Alkaliphilus metalliredigens QYMF. *FEBS Lett* **584**, 3089-3094, doi:10.1016/j.febslet.2010.05.044 (2010).

49 Wu, Y. F. *et al.* Anoxygenic phototrophic arsenite oxidation by a Rhodobacter strain. *Environ Microbiol* **25**, 1538-1548, doi:10.1111/1462-2920.16380 (2023).
50 Trinugroho, J. P. *et al.* Chlorophyll f synthesis by a super-rogue photosystem II complex. *Nature Plants* **6**, 238-244, doi:10.1038/s41477-020-0616-4 (2020).
51 Cardona, T., Murray, J. W. & Rutherford, A. W. Origin and Evolution of Water Oxidation before the Last Common Ancestor of the Cyanobacteria. *Molecular biology and evolution* **32**, 1310-1328, doi:10.1093/molbev/msv024 (2015).
52 Chen, J., Yoshinaga, M., Garbinski, L. D. & Rosen, B. P. Synergistic interaction of glyceraldehydes-3-phosphate dehydrogenase and ArsJ, a novel organoarsenical efflux permease, confers arsenate resistance. *Mol Microbiol* **100**, 945-953, doi:10.1111/mmi.13371 (2016).
53 Lin, Y. F., Walmsley, A. R. & Rosen, B. P. An arsenic metallochaperone for an arsenic detoxification pump. *Proceedings of the National Academy of Sciences* **103**, 15617-15622, doi:10.1073/pnas.0603974103 (2006).
54 Mukhopadhyay, R. & Rosen, B. P. Arsenate reductases in prokaryotes and eukaryotes. *Environ Health Perspect* **110**, 745-748, doi:10.1289/ehp.02110s5745 (2002).
55 Lyons, T. W., Reinhard, C. T. & Planavsky, N. J. The rise of oxygen in Earth's early ocean and atmosphere. *Nature* **506**, 307-315, doi:10.1038/nature13068 (2014).
56 Klatt, J. M., Chennu, A., Arbic, B. K., Biddanda, B. A. & Dick, G. J. Possible link between Earth's rotation rate and oxygenation. *Nature Geoscience 2021 14:8* **14**, 564-570, doi:10.1038/s41561-021-00784-3 (2021).
57 Fru, E. C. *et al.* Arsenic stress after the Proterozoic glaciations. *Sci Rep* **5**, 17789, doi:10.1038/srep17789 (2015).
58 Fru, E. C. *et al.* The rise of oxygen-driven arsenic cycling at ca. 2.48 Ga. *Geology* **47**, 243-246, doi:10.1130/G45676.1 (2019).
59 Chen, S.-C. *et al.* The Great Oxidation Event expanded the genetic repertoire of arsenic metabolism and cycling. *Proceedings of the National Academy of Sciences* **117**, 10414-10421, doi:10.1073/PNAS.2001063117 (2020).
60 Saito, M. A., Sigman, D. M. & Morel, F. M. M. The bioinorganic chemistry of the ancient ocean: the co-evolution of cyanobacterial metal requirements and biogeochemical cycles at the Archean–Proterozoic boundary? *Inorganica Chimica Acta* **356**, 308-318 (2003).
61 Canfield, D. E. A new model for Proterozoic ocean chemistry. *Nature* **396**, 450-453 (1998).
62 Bjerrum, C. J. & Canfield, D. E. Ocean productivity before about 1.9 Gyr ago limited by phosphorus adsorption onto iron oxides. *Nature* **417**, 159-162, doi:10.1038/417159a (2002).
63 Laakso, T. A. & Schrag, D. P. Regulation of atmospheric oxygen during the Proterozoic. *Earth and Planetary Science Letters* **388**, 81-91, doi:10.1016/j.epsl.2013.11.049 (2014).
64 Beer, D., Schramm, A., Santegoeds, C. M., Kühl, M. & Kuhl, M. A nitrite microsensor for profiling environmental biofilms. *Applied and environmental microbiology* **63**, 973-977 (1997).
65 Jeroschewski, P., Steuckart, C. & Kühl, M. An amperometric microsensor for the determination of H2S in aquatic environments. *Analytical Chemistry* **68**, 4351-4357, doi:10.1021/ac960091b (1996).
66 Klatt, J. M. *et al.* Structure and function of natural sulphide-oxidizing microbial mats under dynamic input of light and chemical energy. *The ISME journal* **10**, 921-933, doi:10.1038/ismej.2015.167 (2016).
67 Revsbech, N. P. An oxygen microsensor with a guard cathode. *Limnology and Oceanography* **34**, 474-478, doi:10.4319/lo.1989.34.2.0474 (1989).
68 Castillejos Sepúlveda, A., Gatti, L. M., Kerl, C. F., Chennu, A. & Klatt, J. M. Arsenic speciation analysis in porewater by a novel colorimetric assay. *Science of The Total Environment* **827**, 154155, doi:10.1016/j.scitotenv.2022.154155 (2022).
69 Chennu, A. *et al.* Hyperspectral imaging of the microscale distribution and dynamics of microphytobenthos in intertidal sediments. *Limnology and Oceanography: Methods* **11**, 511-528, doi:10.4319/lom.2013.11.511 (2013).

70 Cronenberg, C., van Groen, B., de Beer, D. & van den Heuvel, H. Oxygen-independent glucose microsensor based on glucose oxidase. *Analytica Chimica Acta* **242**, 275-278, doi:10.1016/0003-2670(91)87075-I (1991).
71 Ousley, S., de Beer, D., Bejarano, S. & Chennu, A. High-resolution dynamics of hydrogen peroxide on the surface of scleractinian corals in relation to photosynthesis and feeding. *Frontiers in Marine Science* **9**, 812839 (2022).
72 Tros, M. *et al.* Breaking the Red Limit: Efficient Trapping of Long-Wavelength Excitati ons in Chlorophyll-f-Containing Photosystem I. *Chem* **7**, 155-173, doi:10.1016/J.CHEMPR.2020.10.024 (2021).
73 Cline, J. D. Spectrophotometric determination of hydrogren sulfide in natural water s. *Limnology and Oceanography* **14**, 454-458, doi:10.4319/lo.1969.14.3.0454 (1969).
74 Bhardwaj, B., Agrawal, A., Ledwani, L., Vaiphei, S. T. & Jain, S. An efficient method for DNA extraction from cyanobacteria isolated from hypersaline and marine environments. *J Phycol* **55**, 733-737, doi:10.1111/jpy.12847 (2019).
75 Bolger, A. M., Lohse, M. & Usadel, B. Trimmomatic: A flexible trimmer for Illumina sequence data. *Bioinformatics* **30**, 2114-2120, doi:10.1093/bioinformatics/btu170 (2014).
76 Li, D., Liu, C.-M., Luo, R., Sadakane, K. & Lam, T.-W. MEGAHIT: an ultra-fast single-node solution for large and complex metagenomics assembly via succinct de Bruijn graph. *Bioinformatics* **31**, 1674-1676, doi:10.1093/bioinformatics/btv033 (2015).
77 Langmead, B. & Salzberg, S. L. Fast gapped-read alignment with Bowtie 2. *Nature Methods* **9**, 357-359, doi:10.1038/nmeth.1923 (2012).
78 Hyatt, D. *et al.* Prodigal: Prokaryotic gene recognition and translation initiation site identification. *BMC Bioinformatics* **11**, 1-11, doi:10.1186/1471-2105-11-119 (2010).
79 Eren, A. M. *et al.* Anvi'o: An advanced analysis and visualization platform for 'omics data. *PeerJ* **2015**, e1319, doi:10.7717/PEERJ.1319/SUPP-5 (2015).
80 Aramaki, T. *et al.* KofamKOALA: KEGG Ortholog assignment based on profile HMM and adaptive score threshold. *Bioinformatics* **36**, 2251-2252, doi:10.1093/bioinformatics/btz859 (2020).
81 Tatusov, R. L., Galperin, M. Y., Natale, D. A. & Koonin, E. The COG database: a tool for genome-scale analysis of protein functions and evolution. *Nucleic Acids Research* **28**, 33, doi:10.1093/NAR/28.1.33 (2000).
82 Buchfink, B., Xie, C. & Huson, D. H. Fast and sensitive protein alignment using DIAMOND. *Nature Methods* **12**, 59-60, doi:10.1038/nmeth.3176 (2015).
83 Blum, M. *et al.* The InterPro protein families and domains database: 20 years on. *Nucleic Acids Research* **49**, D344-D354, doi:10.1093/nar/gkaa977 (2021).
84 Jones, P. *et al.* InterProScan 5: Genome-scale protein function classification. *Bioinformatics* **30**, 1236-1240, doi:10.1093/bioinformatics/btu031 (2014).
85 Sillitoe, I. *et al.* CATH: Expanding the horizons of structure-based functional annotations for genome sequences. *Nucleic Acids Research* **47**, D280-D284, doi:10.1093/nar/gky1097 (2019).
86 Lu, S. *et al.* CDD/SPARCLE: the conserved domain database in 2020. *Nucleic Acids Research* **48**, D265-D268 (2020).
87 Pedruzzi, I. *et al.* HAMAP in 2015: Updates to the protein family classification and annotation system. *Nucleic Acids Research* **43**, D1064-D1070, doi:10.1093/nar/gku1002 (2015).
88 Mi, H., Muruganujan, A., Ebert, D., Huang, X. & Thomas, P. D. PANTHER version 14: More genomes, a new PANTHER GO-slim and improvements in enrichment analysis tools. *Nucleic Acids Research* **47**, D419-D426, doi:10.1093/nar/gky1038 (2019).
89 Bateman, A. *et al.* The Pfam protein families database. *Nucleic Acids Research* **28**, 263-266, doi:10.1093/nar/28.1.263 (2000).
90 Nikolskaya, A. N., Arighi, C. N., Huang, H., Barker, W. C. & Wu, C. H. PIRSF Family Classification System for Protein Functional and Evolutionary Analysis. *Evolutionary Bioinformatics* **2**, 117693430600200, doi:10.1177/117693430600200033 (2006).

91 Attwood, T. K. *et al.* The PRINTS database: A fine-grained protein sequence annotation and analysis resource-its status in 2012. *Database* **2012**, doi:10.1093/database/bas019 (2012).
92 Sigrist, C. J. A. C. J. A. *et al.* New and continuing developments at PROSITE. **41**, D344-D347, doi:10.1093/nar/gks1067 (2012).
93 Letunic, I. & Bork, P. 20 years of the SMART protein domain annotation resource. *Nucleic Acids Research* **46**, D493-D496, doi:10.1093/nar/gkx922 (2018).
94 Brown, S. *et al.* The Structure-Function Linkage Database. *The FASEB Journal* **20**, doi:10.1096/fasebj.20.5.a899-c (2006).
95 Pandurangan, A. P., Stahlhacke, J., Oates, M. E., Smithers, B. & Gough, J. The SUPERFAMILY 2.0 database: A significant proteome update and a new webserver. *Nucleic Acids Research* **47**, D490-D494, doi:10.1093/nar/gky1130 (2019).
96 Haft, D. H. *et al.* TIGRFAMs and genome properties in 2013. *Nucleic Acids Research* **41**, doi:10.1093/nar/gks1234 (2013).
97 Camacho, C. *et al.* BLAST+: Architecture and applications. *BMC Bioinformatics* **10**, 1-9, doi:10.1186/1471-2105-10-421/FIGURES/4 (2009).
98 Kang, D. D. *et al.* MetaBAT 2: An adaptive binning algorithm for robust and efficient genome reconstruction from metagenome assemblies. *PeerJ* **2019**, e7359, doi:10.7717/PEERJ.7359/SUPP-3 (2019).
99 Wu, Y.-W., Simmons, B. A. & Singer, S. W. MaxBin 2.0: an automated binning algorithm to recover genomes from multiple metagenomic datasets. *Bioinformatics* **32**, 605-607, doi:10.1093/bioinformatics/btv638 (2016).
100 Chaumeil, P. A., Mussig, A. J., Hugenholtz, P. & Parks, D. H. GTDB-Tk: a toolkit to classify genomes with the Genome Taxonomy Database. *Bioinformatics* **36**, 1925-1927, doi:10.1093/BIOINFORMATICS/BTZ848 (2020).
101 Parks, D. H. *et al.* A standardized bacterial taxonomy based on genome phylogeny substantially revises the tree of life. *Nature Biotechnology* **36**, 996-1004, doi:10.1038/nbt.4229 (2018).
102 Woodcroft, B. J. & Newell, R. wwood/CoverM: Read coverage calculator for metagenomics. (2021).
103 Wickham, H. *ggplot2: Elegant Graphics for Data Analysis*. (Springer-Verlag New York, 2016).
104 Team, R. C. R: A Language and Environment for Statistical Computing. (2020).
105 Bushnell, B. BBMap short-read aligner, and other bioinformatics tools. (2015).
106 Wagner, G. P., Kin, K. & Lynch, V. J. Measurement of mRNA abundance using RNA-seq data: RPKM measure is inconsistent among samples. *Theory in Biosciences* **131**, 281-285, doi:10.1007/s12064-012-0162-3 (2012).
107 Kolde, R. CRAN - Package pheatmap. (2019).
108 Ordóñez, E. *et al.* Arsenate reductase, mycothiol, and mycoredoxin concert thiol/disulfide exchange. *Journal of Biological Chemistry* **284**, 15107-15116 (2009).
109 Páez-Espino, D., Tamames, J., Lorenzo, V. & Cánovas, D. Microbial responses to environmental arsenic. *BioMetals* **22**, 117-130, doi:10.1007/s10534-008-9195-y (2009).
110 Silver, S. & Phung, L. T. Genes and enzymes involved in bacterial oxidation and reduction of inorganic arsenic. *Applied and environmental microbiology* **71**, 599-608, doi:10.1128/AEM.71.2.599-608.2005 (2005).